Peak factor statistics of wind effects for hyperbolic paraboloid roofs

Fabio Rizzo[a], Michele Barbato[b,*], Vincenzo Sepe[a]

[a] University "G. D'Annunzio" of Chieti-Pescara, Viale Pindaro 42, 65127 Pescara, Italy
[b] Louisiana State University, 3230B Patrick F. Taylor Hall, Baton Rouge, LA 70803, USA

ARTICLE INFO

ABSTRACT

This paper investigates the statistics of the pressure coefficients and their peak factors in hyperbolic paraboloid roofs that are commonly used in tensile structures. The experimental peak factor statistics, estimated using pressure coefficient time histories experimentally measured in wind tunnel tests, were compared with the corresponding peak factor statistics estimated through the use of six analytical models available in the literature, namely the Davenport, classical Hermite, revised Hermite, modified Hermite, Translated-Peak-Process (TPP), and Liu's models. The basic assumption of the TPP model, i.e., that the pressure coefficient local peaks follow a Weibull distribution, was validated and was used to estimate analytically the peak factors' quantiles. Different time history durations and different error measures were also considered. The non-Gaussian properties of the pressure coefficient processes were characterized at different roof locations for different wind angles of attack. It was found that: (1) the region of non-Gaussianity is significantly affected by the wind angle; (2) as expected, the Davenport model underestimates the peak factor mean and standard deviation in regions of high non-Gaussianity; (3) the modified Hermite model provides the best estimates overall of the peak factor mean; and (4) the TPP model provides the best estimates overall of the peak factor standard deviation. In addition, the modified root mean squared error was found to provide the most reliable assessment of the analytical models' accuracy among the different error measures considered in this study.

1. Introduction

Tensile structures are widely used for hyperbolic paraboloid roofs (HPRs). This structural typology is frequently used for multi-functional buildings that require large interior open spaces [1], since they allow covering extremely large spans (up to 150 m, as for example The Khan Shatyr Entertainment Centre in Kazakhstan, completed in 2010) without intermediate pillars in a cost-effective manner. In addition, they are lighter than other structural typologies for similar spans and, thus, permit a wider selection of design solutions.

These structures present the unique feature that their load-bearing elements (i.e., cables and membranes) sustain pure tension and, thus, resist very efficiently external loads [2–4]. These load-bearing elements are very flexible and generally experience large deflections. Thus, the initial structural equilibrium configuration needs to be optimized through the appropriate distribution of permanent loads and a careful selection of the geometric shape. The most commonly used shape for tensile structures is the hyperbolic paraboloid, which has been employed in many structures around the world, e.g., the Olympiastadion in Munich, Germany (designed by Otto Frei and completed in 1968) and the Denver Union Station roof in Denver, CO (USA)

(completed in 2013). The hyperbolic paraboloid is an elementary double curvature surface, nowadays usually realized by means of two series of parallel cables, one series oriented upward and the other downward. For load combinations controlled by gravity loads (e.g., self-weight, dead and snow loads), the upward cables act as load-bearing cables, whereas the downward cables are stabilizing cables. However, under suction due to wind loads, the upward cables provide the stabilizing action, whereas the downward cables resist the wind loads.

Because of their lightness and deformability, the stability of tensile structures and in particular of hyperbolic paraboloid cable nets is extremely sensitive to their aerodynamic and aeroelastic response under wind actions. However, knowledge of these aerodynamic and aeroelastic behaviors is limited [2]. In addition, existing technical codes provide design guidelines only for static loading conditions and/or temporary structures [5–7]. These code prescriptions are backed up by several manuals of practice, which examine in depth several aspects related to the design of tensioned fabric roofs [8,9]. In this context, the European Network for Membrane Structures "TensiNet" developed the TensiNet Design Guide [10], which is widely considered the state-of-the-art guide for the design of tensile structures and also provides a few

---

* Corresponding author.
  E-mail addresses: fabio.rizzo@unich.it (F. Rizzo), mbarbato@lsu.edu (M. Barbato), v.sepe@unich.it (V. Sepe).

examples of aerodynamic wind actions on tensile structures [4].

It is noted here that HPRs have been used in the past also for low-flexibility shell structures made of light reinforced concrete (e.g., the Olympic Saddledome in Calgary and several buildings designed by Mexican architect Felix Candela [11]), and for medium-flexibility lattice structures constructed with plywood [12]. For these stiffer structural typologies, the aerodynamic behavior is predominant, whereas the aeroelastic behavior has a smaller influence on the structural design. For flexible HPRs consisting of tensile structures, both aerodynamic and aeroelastic behaviors are equally important and their characterization for design purposes requires an iterative two-phase approach in which the results of two separate analyses (performed numerically or experimentally in wind tunnels) are interdependent [13]. However, the pressure coefficients can be accurately estimated using rigid models in wind tunnel tests even for flexible HPRs, since the deflections of well-designed structures need to satisfy code requirements and are generally too small to affect the pressure coefficients [14].

The importance of the aerodynamic behavior of HPRs has been recognized in a few recent studies that investigated the dynamic behavior [14–18] and the distribution of pressure coefficients on different geometries [19–26]. It is noteworthy that peak pressure coefficients (usually expressed in terms of peak factors) are crucial to estimate peak loads [27], which for this type of structure could be related to local and global critical conditions. In addition, modern performance-based reliability design approaches require the accurate estimation of extreme wind loads and their distribution [28–30].

In principle, the peak factor's distribution can be obtained based on the classical extreme value theory [31]. If the process is Gaussian, the Davenport equations provide satisfactory estimates of the mean and standard deviation of the peak factor [32,33]. If the process is non-Gaussian, no exact solution exists to predict mean and standard deviation of the peak factors. In general, using a Gaussian approximation yields non-conservative peak factor values when applied to non-Gaussian processes [34,35].

Several analytical models have been proposed in the scientific literature to predict non-Gaussian load effects. Kareem and Zhao [34] proposed an analytical expression for the mean of non-Gaussian peak factors using a moment-based model [31] based on the concept of non-Gaussian translation process [36] with a cubic Hermite polynomial transformation. Winterstein et al. [37] proposed a modification of the Davenport equation for the non-Gaussian peak factor mean by including the effects of clustering. Sadek and Simiu [38] proposed an automated mapping procedure to estimate the peak distribution of wind-induced non-Gaussian internal forces on low-rise buildings by using a database-assisted design software. This mapping procedure requires identifying an analytical marginal probability distribution for the time series of interest through numerical fitting of the distribution parameters. However, the Sadek–Simiu method has been applied only to non-Gaussian processes with an underlying marginal gamma distribution [39–43].

Kwon and Kareem [27] derived an analytical solution for the non-Gaussian peak factor standard deviation based on the Hermite model and proposed a revised Hermite model and a modified Hermite model for estimating the mean and standard deviation of non-Gaussian peak factors. The revised Hermite model is based on the optimal parameters of a four-moment cubic Hermite polynomial transformation [44]; however, this model has some validity limitation regarding the specific ranges of the skewness and kurtosis of the process. The modified Hermite model is based on an equivalent statistical cubicization procedure [45,33] and requires solving of a system of coupled nonlinear equations that depend on the skewness and kurtosis of the process. Huang et al. [42] proposed the Translated-Peak-Process (TPP) model to estimate the local peak distribution, peak factors, and quantiles of peak extremes. The TPP model is a modification of the Sadek-Simiu point-to-point mapping procedure, which assumes a Weibull distribution for the local

peaks of non-Gaussian process' time histories. The TPP model was validated by comparing the analytical estimates with wind-tunnel pressure experimental results for a tall building. Ma and Xu [46] proposed a moment-based Johnson transformation method in conjunction with a Gumbel distribution assumption to estimate the statistics of wind pressure peak factors. The results of this method were validated through a comparison with the peak factors obtained from long-duration pressure records measured in wind-tunnel tests on the model surfaces of a high-rise building. It is noted here that, while there is an agreement in the literature that the Davenport model tends to underestimate (sometimes significantly) the mean value of the peak factors, there is no agreement on a single best model for all structures, with different versions of the Hermite model that seem to perform better for roof of low-rise buildings [27,42,47], and other approaches that seem to be preferable for the vertical sides of tall buildings [42,46].

Validation of the peak statistics' estimation models available in the literature is extremely limited for HPRs. Ding and Chen [21] compared the accuracy of various methods for extreme value analysis, (i.e., the peaks-over-threshold method, the average conditional exceedance rate method, and the translation process method with various translation models, including the Hermite model) for select pressure taps' recordings obtained from a wind tunnel test on a saddle-type HPR. Liu et al. [23] investigated different statistics of dynamic pressures on a saddle-type HPR, as well as the dependence of these statistics on different turbulence profiles. They observed that the peak factors in the flow separation regions presented a significant non-Gaussian behavior and that moment-based Hermite estimates were accurate only for mild non-Gaussianity. Liu et al. [24] proposed a new version of the Hermite model, in which modified moments of the original process are used to estimate separately the means of positive and negative peak factors. This model (referred to as the Liu's model hereafter) was verified through a comparison with the peak factors of wind pressures measured in wind tunnel tests on a large-span saddle-type roof. It is noteworthy that the roof considered in [23,24] is representative only of HPRs with linear edges (i.e., inclined at 45° with respect to the sagging and hogging directions of the roof). The extreme values of the pressure coefficients on HPRs are significantly affected by turbulence [23] and roof shape [19,20]. However, information on appropriate ranges and/or models for HPRs is lacking in current technical standards and design codes [48–56]. In addition, there is a need for a detailed comparison of the different analytical models available in the literature in terms of their accuracy in estimating the statistics of wind pressure peak factors for HPRs. It is also noted that, while many studies available in the literature investigate the accuracy of analytical models for individual wind pressure recordings (i.e., single pressure tap and single duration), only few of them investigate the overall accuracy of these models for a given surface, e.g., [42,46] for the vertical sides of tall buildings, and [47] for the roof of low-rise buildings. Moreover, in these investigations different types of errors have been used to quantify the accuracy of different models, and it is not immediately apparent how the results obtained using different error definitions can be compared. Finally, the authors of the present paper were not able to identify studies that take into consideration the effects of different durations of the wind pressure recordings.

Based on an extensive wind-tunnel experimental campaign, the research presented in this paper investigates in detail the statistics of the peak factors in HPRs, as well as the non-Gaussian properties of the peak factors as functions of the position on a square HPR and the relative direction of the wind. This study also investigates the overall relative accuracy of different analytical models for the estimation of peak factor statistics when compared with experimental wind tunnel measurements on a scaled model of a building with a square HPR. This accuracy is investigated for different lengths of the pressure time histories and for different definitions of error.

2. Research relevance

This study provides several new contributions to the field of Structural Wind Engineering. In particular, it provides a better understanding of the Gaussian and non-Gaussian behavior of the local pressure coefficient processes on HPRs, as well as the effect of non-Gaussianity on the peak factor's statistical moments for this structural geometry. This understanding is a necessary step toward the development of modern design guidelines for tensile structures using hyperbolic paraboloid shapes. This study also develops a better understanding of the effects of different time durations with respect to the accuracy of different analytical models for the estimation of the peak factor's statistics. The knowledge of the different models' performance over different time durations allow the identification of which models can be reliably used to extrapolate the peak factor's statistics beyond the time durations that are compatible with specific wind tunnel tests. Finally, to the best of the authors' knowledge, this study presents the first careful comparison of different error measures used to compare the performance of different analytical models. The identification of an appropriate error measure, particularly when considering average errors over an entire surface equipped with numerous pressure taps in wind tunnel tests, can provide important guidance for future experimental and numerical studies to investigate the statistics of pressure coefficients and peak factors for different surface geometries.

3. Description of the model geometry and wind tunnel tests

Wind tunnel testing was carried out in the CRIACIV's open circuit boundary layer wind tunnel in Prato, Italy [19], with a test chamber size 2.3 m × 1.6 m. The test used in this research was performed on a square wood model of HPR with the following geometric parameters: $L_1 = L_2 = 80$ cm = model lengths in the sagging (upward curvature) and hogging (downward curvature) directions, respectively (corresponding to the cable spans of the roof); $f_1 = 2.67$ cm = model sag in the sagging direction; $f_2 = 5.33$ cm = model sag in the hogging direction; $H_1 = 13.33$ cm = height of the lowest roof point in the sagging direction; and $H_2 = 21.33$ cm = height of the highest roof point in the hogging direction (Fig. 1). It is observed that this model is different from that considered in [23,24], because it has curved edges instead of linear edges, i.e., the sides of the square plan coincide with the roof's sagging and hogging directions.

The wind directions considered in the wind tunnel tests are indicated in Fig. 1. The direction corresponding to a wind angle of attack θ = 0° is parallel to the hogging direction, whereas the direction corresponding to θ = 90° is parallel to the sagging direction of the roof.

A picture of the rigid wood model tested in the wind tunnel is shown in Fig. 2. The wood model was fitted with 181 pressure taps on the lateral surfaces and 89 pressure taps on the roof. All pressure taps were connected to pressure scanners through polytetrafluoroethylene tubes, calibrated to obtain a flat frequency response in the range of interest (from 0 to 100 Hz).

The roof pressure taps were distributed according to the map shown in Fig. 3, which also shows five different significant roof portions, referred to as zone A through zone E. Zone A is the edge detachment zone for θ = 0°, zone B is the edge detachment zone for θ = 90°, zone C
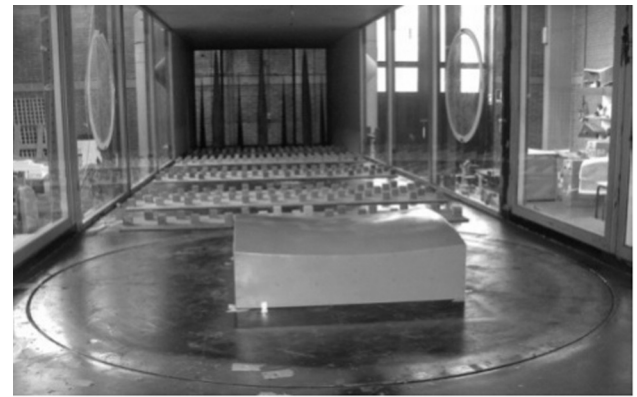

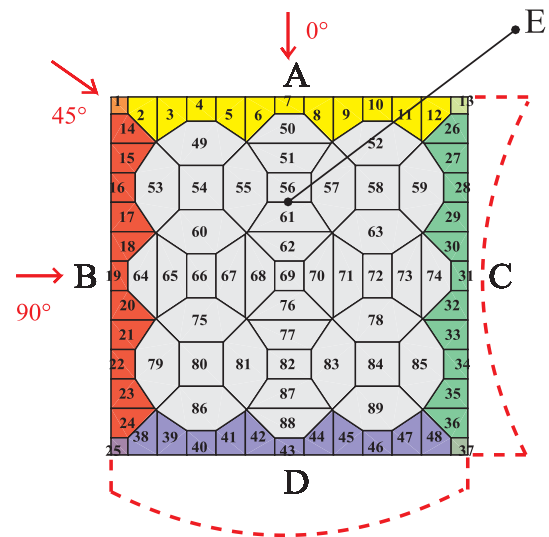**Fig. 2.** In-scale wind tunnel physical model.

Fig. 3. Pressure taps' location and zone identification on the HPR.

represents the roof edge parallel to zone B, zone D represents the roof edge parallel to zone A, and zone E corresponds to the central portion of the roof. The wind tunnel tests were performed with an average wind speed of 16.7 m/s at a height of 10 cm, a sampling frequency equal to 252 Hz and an acquisition time $T_0 = 30$ s. The recording duration corresponds to an equivalent-time duration of approximately 30 min when considering a scale 1/100 for the physical model with respect to a full-scale structure. Additional information on the test setup and results can be found in [19], where the average pressure coefficients on the roof and walls were presented for several geometrical models of HPRs. The experimental results of relevance for the present study are reported in the following section of this paper.

4. Experimental results

Results based on the experimental campaign described in [19,22] are shown in Figs. 4–7. Figs. 5–7 report relevant statistics of the wind tunnel experimental results for θ = 0°, 45°, and 90°, respectively, calculated over the entire duration of the recorded time-histories, i.e., for $T_0 = 30$ s, by assuming that the underlying process is stationary. In particular, the different subfigures present the mapping for all pressure taps of the following pressure coefficient's statistics: (a) mean, μ_{c_p} (previously reported in Rizzo et al. [19] but repeated here for the sake of completeness); (b) standard deviation, σ_{c_p}; (c) skewness coefficient, γ_{c_p}; (d) excess kurtosis, κ_{c_p}; (e) mean zero-crossing rate, ν_0 (obtained as the average between the total up-crossings and down-crossings of the zero level divided by the record duration, e.g., see [21,57]); and (f)
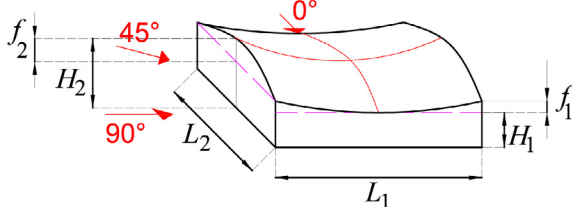

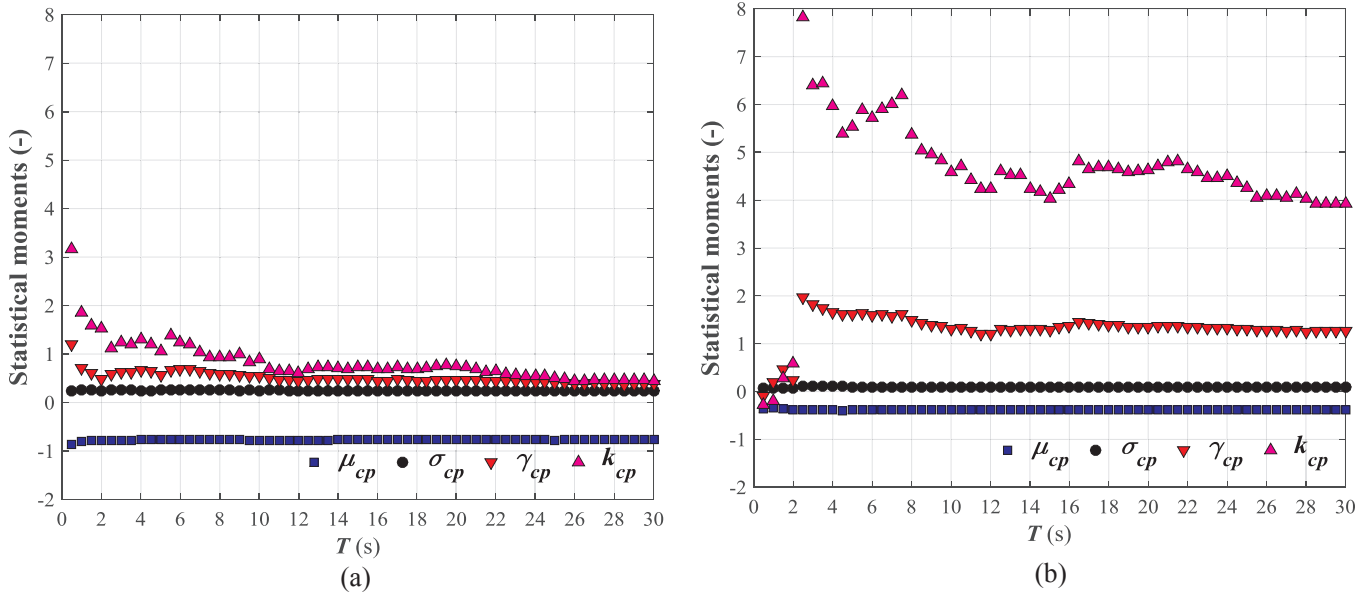**Fig. 1.** Geometry of the hyperbolic paraboloid model.

Fig. 4. Values of the pressure coefficient's mean, standard deviation, skewness, and excess kurtosis as functions of the experimental record's time duration: (a) pressure tap #11 for θ = 0°, and (b) pressure tap #5 for θ = 90°.

peak factor, g_{T_0}. Standard deviation, skewness coefficient, and excess kurtosis are scaled up by a factor equal to 10 for the sake of presentation clarity.

In this study, positive values of the pressure coefficients correspond to suction (i.e., to a pressure lower than the static pressure of the undisturbed wind flow, p_0). Thus, the time variant pressure coefficient at the i-th pressure tap ($i = 1, \ldots, 89$) is given by:

$$c_{p,i}(t) = \frac{p_0 - p_i(t)}{\frac{1}{2}\rho \cdot V_m^2} \tag{1}$$

where $p_i(t)$ denotes the wind pressure measured at time t for pressure tap i on the roof surface, ρ denotes the air density, and V_m denotes the mean speed of the undisturbed wind flow. It is noted here that higher-order statistical moments (i.e., skewness and excess kurtosis) have higher variability than lower-order statistical moments (i.e., mean and standard deviation), particularly for non-Gaussian processes [58]. This phenomenon is related to the need to achieve approximate stationarity of the underlying process in order to obtain reliable estimates of the statistical moments. In order to identify potential inaccuracies in the estimates of higher-order moments, the variability of these statistical moments was investigated as a function of the duration of the time interval over which they were estimated. For all pressure taps and all directions considered in this investigation, it was found that in almost all cases: (1) the pressure coefficient's means and standard deviations converged before 5 s of recorded time histories, (2) the pressure coefficient's skewness converged before 22 s of recorded time histories, and (3) the pressure coefficient's excess kurtosis converged before 27 s of recorded time histories. Fig. 4 shows the values of the pressure coefficient's mean, standard deviation, skewness, and excess kurtosis as functions of the experimental record's time duration for two representative pressure taps (i.e., pressure taps 11 and 5 for wind angles θ = 0° and 90°, respectively). Based on these results, it is concluded that the values of the pressure coefficient's statistical moments (in particular, skewness and excess kurtosis) correspond to the converged constant values for the underlying stationary processes.

It is observed that the mean pressure coefficients assume positive values at all locations for all three wind angles of attack, i.e., the wind action on the roof overall correspond to a suction force. However, for a few pressure taps, negative values of the pressure coefficients (i.e., pressures that are higher than p_0) were recorded for short portions of

the time histories. With the exceptions of mean and standard deviations of the pressure coefficients, all calculations were performed after the signals were subtracted from their corresponding mean values and normalized by their corresponding standard deviations (to obtain a zero-mean process with unit standard deviation, see, e.g., [27]). The experimental results are presented in the following subsections for each of the considered wind angles of attack.

4.1. Statistics of pressure coefficients for wind angle of attack θ = 0°

For θ = 0°, the mean pressure coefficients vary significantly with the location of the pressure tap, with values ranging from 1.332 to 0.192 (Fig. 5a). The values of the mean pressure coefficients are highest along the edge detachment zone A, after which they drop immediately to low values, slightly increase toward the middle of the roof and then decrease again to the lowest values in zone D. The standard deviations of the pressure coefficients assume their highest values in zone A with the maximum value equal to 0.367, their intermediate values in zones B and C, and their lowest values in zones D and E, with the minimum value equal to 0.040 (Fig. 5b).

The skewness coefficient (Fig. 5c) and excess kurtosis (Fig. 5d) exhibit a very similar trend, i.e., they are generally highly correlated. In fact, they assume their highest positive values toward the middle of zones B and C (1.486 for the skewness coefficient and 7.236 for the excess kurtosis, respectively), intermediate positive values in the reminder of zones B and C as well as in zone A, and low-magnitude positive or negative values in zones D and E (with the minimum values equal to −0.098 for the skewness coefficient and −0.374 for the excess kurtosis, respectively). According to [59], the roof regions where the pressure coefficient process is non–Gaussian are identified by $|\gamma_{c_p}| > 0.5$ and/or $|\kappa_{c_p}| > 0.5$. Based on this criterion and the results reported in Fig. 5c and d, the considered process is non-Gaussian in most of the pressure taps located in zones A, B, and C.

The mean zero-crossing rate presents a smaller variability than other statistics, with the maximum and minimum values equal to 15.989 Hz and 8.364 Hz, respectively (Fig. 5e). The largest values for ν_0 are observed in zones A, B, and C. The peak factors show a trend similar to that of the mean zero-crossing rate. In this case, the largest values for the peak factors (with the maximum value equal to 10.298) are observed near the middle of zones B and C, i.e., near the highest portions of the roof (Fig. 5f), which correspond also to the zones with the largest

Fig. 5. Statistics of wind pressure coefficients for θ = 0°: (a) mean, μ_{c_p}; (b) standard deviation (scaled up by 10), σ_{c_p}; (c) skewness coefficient (scaled up by 10), γ_{c_p}; (d) excess kurtosis (scaled up by 10), κ_{c_p}; (e) mean zero-crossing rate, ν_0 (Hz); and (f) peak factor, g_{T_0}.

Fig. 6. Statistics of wind pressure coefficients for θ = 45°: (a) mean, μ_{cp}; (b) standard deviation (scaled up by 10), σ_{cp}; (c) skewness coefficient (scaled up by 10), γ_{cp}; (d) excess kurtosis (scaled up by 10), κ_{cp}; (e) mean zero-crossing rate, ν_0 (Hz); and (f) peak factor, g_{T0}.
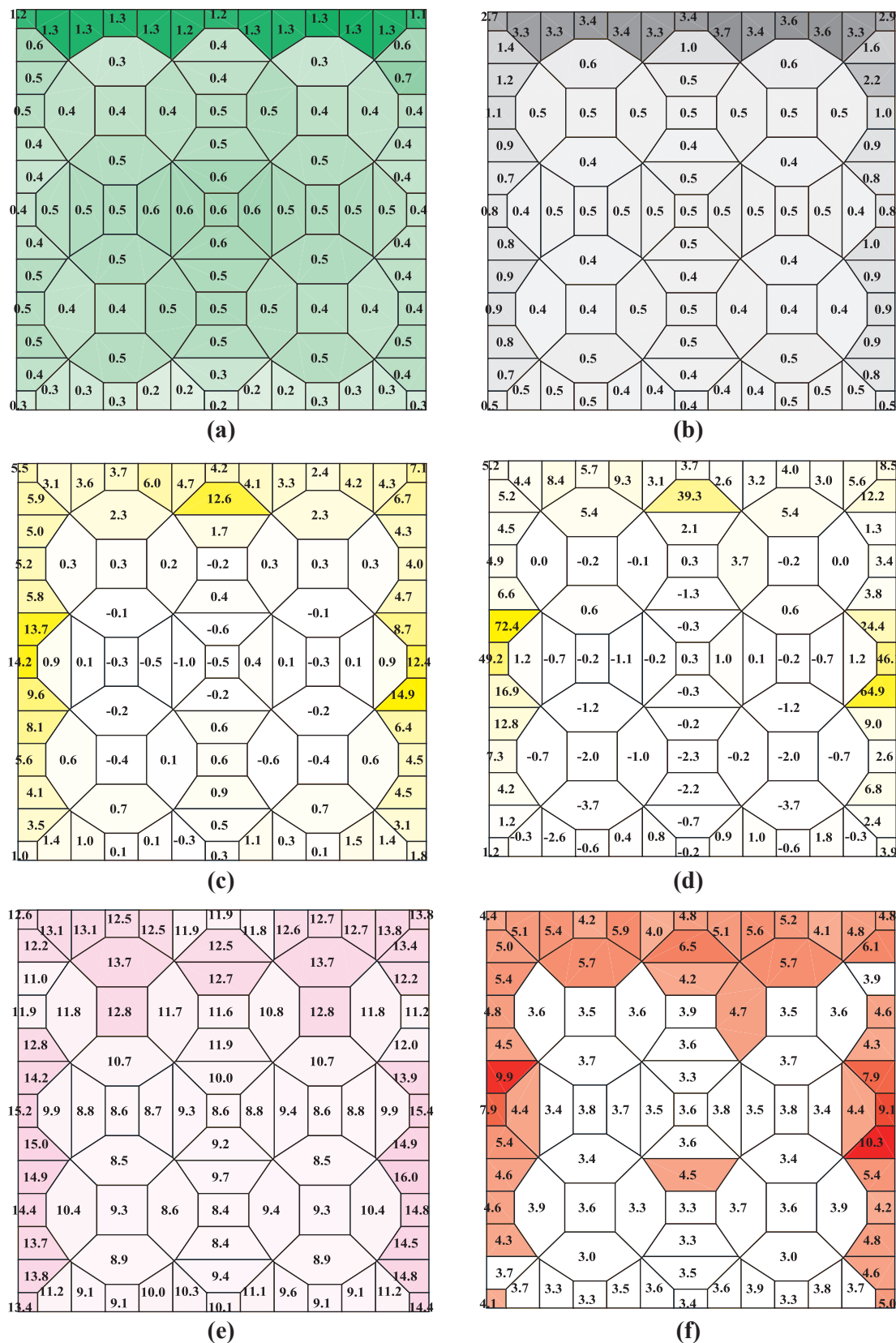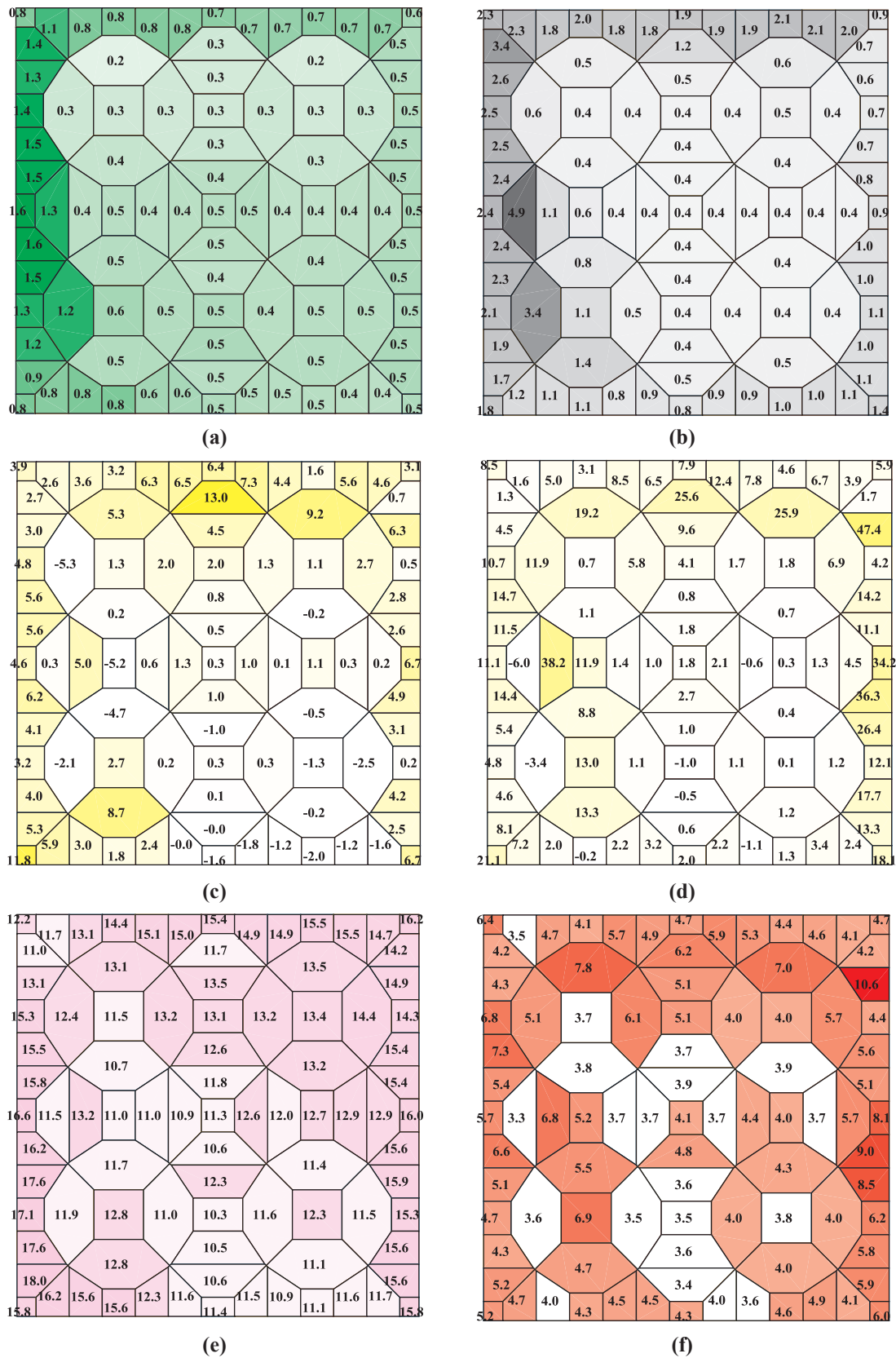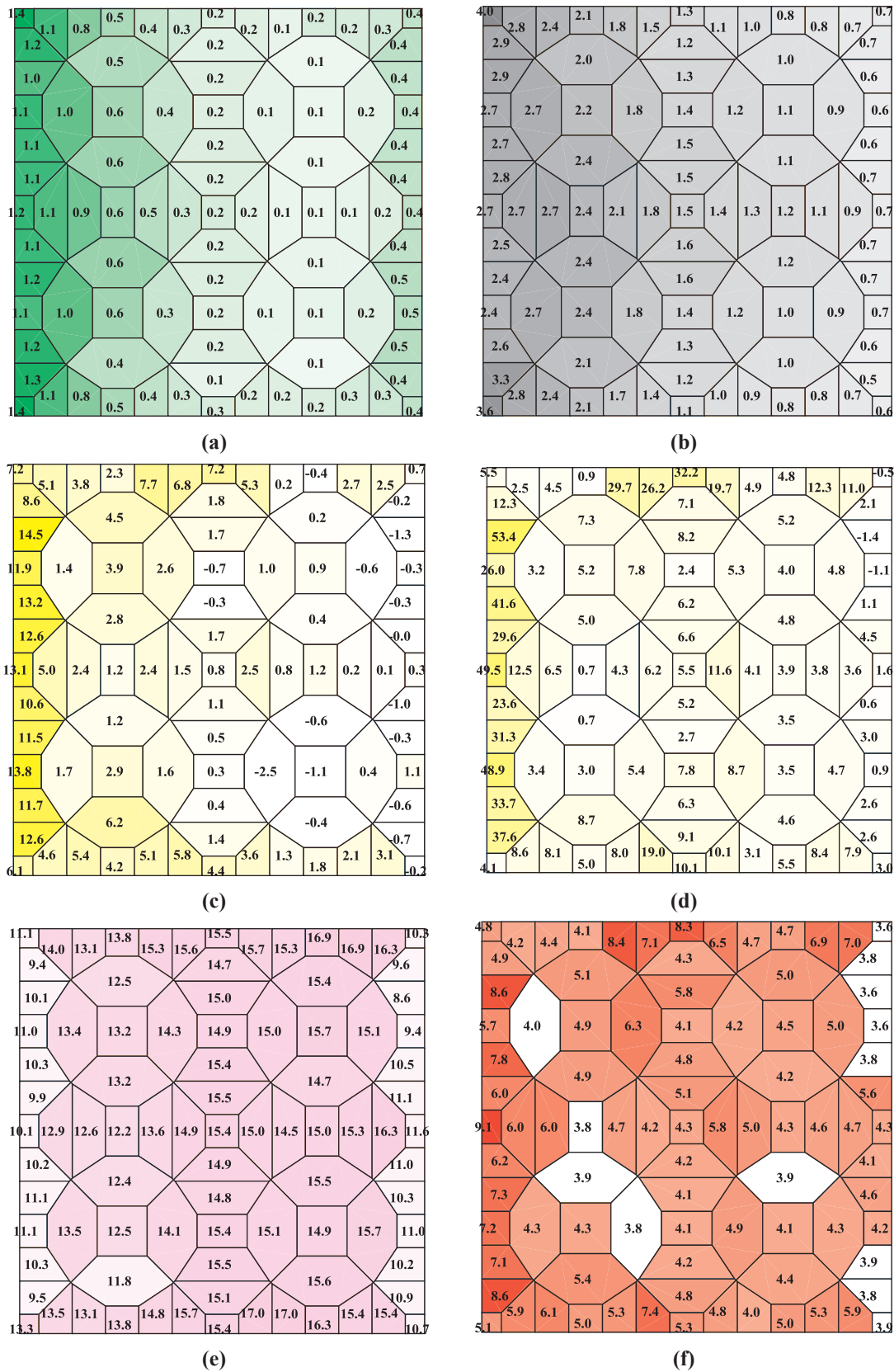
Fig. 7. Statistics of wind pressure coefficients for θ = 90°: (a) mean, μ_{cp}; (b) standard deviation (scaled up by 10), σ_{cp}; (c) skewness coefficient (scaled up by 10), γ_{cp}; (d) excess kurtosis (scaled up by 10), κ_{cp}; (e) mean zero-crossing rate, ν_0 (Hz); and (f) peak factor, g_{T0}.

values of the skewness coefficient and excess kurtosis. Relatively large values of the peak factors (in the range 4.0–6.5) are observed in the remainders of zones B and C, in zone A, and in the portion of zone E immediately near to zone A. The peak factors assume values close to 3.5 in most of zone E and in zone D, i.e., in the roof region where the process describing the pressure coefficient can be considered Gaussian. It is noteworthy that a value of 3.4 to 3.5 for the peak factor is often used in design applications [52], based on the assumption that the underlying process is Gaussian. The observed maximum and minimum values of the peak factor are equal to 10.298 and 2.987, respectively.

As expected from the geometry of the roof and the wind flow, the trends for all the considered statistics are almost symmetric with respect to the centerline of the roof that is parallel to the hogging direction. It is also observed that non-Gaussianity appears to be not necessarily correlated with the magnitude of the pressure coefficients' mean and standard deviation.

4.2. Statistics of pressure coefficients for wind angle of attack $\theta = 45°$

For $\theta = 45°$, the mean pressure coefficients are slightly higher than those for $\theta = 0°$ and vary between 1.607 and 0.161 (Fig. 6a). The highest values of the mean pressure coefficients are observed near the detachment zone along the hogging direction (zone B and part of zone E). The maximum value is reached at the highest point of the roof in zone B. Zone A contains the intermediate values of the mean pressure coefficients, whereas zones C, D, and E have smaller values.

The standard deviations of the pressure coefficients assume their highest values also in zone B and part of zone E, with the maximum value equal to 0.491 observed at pressure tap #64, i.e., in zone E next to the pressure tap located at the highest point of the roof (Fig. 6b). The standard deviations of the pressure coefficients assume intermediate values in zone A and smaller values in the remainder of the roof, with the minimum value equal to 0.035.

The skewness coefficient assumes its highest values near the lowest point of the roof from the side of attack for the wind, i.e., toward the middle of zone A and the neighboring portion of zone E, as well as at the far corner of zone B (Fig. 6c). The maximum value is equal to 1.299 and is observed at pressure tap #50. Several pressure taps in zone D and E have negative skewness coefficients, with values as low as −0.529. The excess kurtosis assumes large values in zone B with the exclusion of the corners and in the middle of zones A and (in minor measure) D (Fig. 6d). The maximum value is 4.744 and is observed at pressure tap #27. Lower values are generally observed in zone D, where negative values are measured at a few pressure taps. However, the lowest value of −0.601 is achieved at pressure tap #64, in zone E next to zone B. It is also observed that a significant portion of the pressure taps of the roof have excess kurtosis values larger than 0.50, which is the conventional value suggested in [59] above which the pressure coefficient process can be considered non-Gaussian.

The mean zero-crossing rate presents larger values around the edges defined by zones A, B, and C, with values as high as 18.038 Hz, and smaller values elsewhere, with values as low as 10.278 Hz (Fig. 6e). The peak factors assume values higher than 4.0 in most of the pressure taps, with the highest values observed in zone C and the maximum value equal to 10.570 achieved at pressure tap #27 (Fig. 6f). The minimum value of the peak factor is equal to 3.319 and is measured at pressure tap #64 in zone E. For this wind angle of attack, the relatively high values of the peak factors seem to confirm the previous observation, based only on the values of skewness coefficient and excess kurtosis, that the pressure coefficient process is non-Gaussian on most of the roof.

4.3. Statistics of pressure coefficients for wind angle of attack $\theta = 90°$

For $\theta = 90°$, the mean pressure coefficients are lower than for $\theta = 45°$ and have a slightly higher variability than those for $\theta = 0°$. The

highest values are achieved in zone B, with the maximum value equal to 1.426 at pressure tap #1 (i.e., at the corner near zone A, see Fig. 7a). The mean pressure coefficients decrease slowly moving from zone B through zone E, where the minimum value of 0.090 is achieved, and then increase again in zone C. The standard deviations of the pressure coefficients follow a trend similar to that of the mean pressure coefficients (Fig. 7b). In fact, they assume their largest values overall in zone B, even though the maximum value equal to 0.397 is observed in pressure tap #64 (i.e., zone E). The standard deviations then gradually decrease moving from the detachment edge to the other side of the roof, with the lowest values overall in zone E.

The skewness coefficient assumes its highest positive values near the detachment edge in zone B, with the maximum value equal to 1.454 at pressure tap #15 and all values above the Gaussianity threshold of 0.5 (Fig. 7c). The skewness coefficient assumes intermediate positive values, only few of which are above the Gaussianity threshold of 0.5, along the two edges that are parallel to the wind flow (i.e., zones A and D). It reaches the lowest values in zones C and E, with the minimum equal to −0.249 at pressure tap #83. It is also observed that, in zones C and E, the skewness coefficient is negative only at a few of the pressure taps and is higher in absolute value than the Gaussianity threshold of 0.5 only at two pressure taps. The excess kurtosis follows a trend similar to that of the skewness coefficient, with the highest values in zone B and the maximum value of 5.345 at pressure tap #15, intermediate values in zones A and D, and lowest values in zones C and E (Fig. 7d). The minimum value is equal to −0.143 and is reached at pressure tap #27. Only three pressure taps, all located in zone C, have negative values of excess kurtosis. More than half of the pressure taps present an excess kurtosis higher in absolute value than the Gaussianity threshold of 0.5, i.e., in most of the roof the pressure coefficient process can be considered non-Gaussian.

The mean zero-crossing rate presents larger values in zones A, D, and E and lower values at the two edges orthogonal to the wind flow (Fig. 7e), with the maximum value equal to 16.997 Hz and the minimum value equal to 8.632 Hz. The peak factors assume values higher than 4.0 in almost all the pressure taps, with the exception of 13 pressure taps, of which eight are located in zone C and 5 in zone E (Fig. 7f). The highest values are reached along the detachment edge in zone B, where the maximum value is equal to 9.093 at pressure tap #19 (i.e., at the highest point of the roof), and along the two sides parallel to the wind flow (i.e., zones A and D). The minimum value is equal to 3.573 and is achieved at pressure tap #27 in zone C. For this wind angle of attack, the overall high values of the peak factors are consistent with the high values of skewness coefficient and excess kurtosis and indicate that the pressure coefficient process is non-Gaussian on most of the roof.

5. Analytical estimates of peak factor statistics

This section briefly describes six different analytical models for the statistics of the peak factor, which have been proposed in the literature, namely the Davenport [32], classical Hermite [27,34], revised Hermite [27], modified Hermite [27], TPP [42], and Liu's [24] models. The peak factor statistics considered in this study are: (1) the mean value, $\mu_{g,M}(T)$; (2) the standard deviation, $\sigma_{g,M}(T)$; and (3) the α-quantile, $X_{g,M}^{\alpha}(T)$; in which α denotes the quantile rank, i.e., $\alpha = P[g_T \leqslant X_{g,M}^{\alpha}(T)]$, where $P[\cdots]$ denotes the probability of the event defined in the square brackets; M = D (for Davenport model), H (for classical Hermite model), rH (for revised Hermite model), mH (for modified Hermite model), TPP (for TPP model), or L (for Liu's model); and T denotes the time interval of reference.

5.1. Davenport model

The Davenport peak factor statistics are based on the assumption that the underlying process is Gaussian [32]. The distribution of the

local peaks (i.e., local maxima in time) of a standardized Gaussian process reduces to the Rayleigh distribution for narrow-band processes [60]. Davenport peak factor is often employed in wind engineering practice [52] to estimate the mean extreme value (i.e., the mean value of the global maximum in time) of wind-induced responses. The statistics of the Davenport peak factor are given by [32]:

$$\mu_{g,D}(T) = \beta + \frac{\gamma}{\beta} \tag{2}$$

$$\sigma_{g,D}(T) = \frac{\pi}{\beta\sqrt{6}} \tag{3}$$

$$X_{g,D}^{\alpha}(T) = \sqrt{2\ln(\nu_0 \cdot T) - 2\ln(-\ln\alpha)} \tag{4}$$

in which $\gamma \approx 0.5772$ is the Euler's constant, and $\beta = \sqrt{2\ln(\nu_0 \cdot T)}$. Eq. (4) is derived here directly from the distribution of the largest peak value presented in [32].

5.2. Hermite models

The classical, revised, and modified Hermite models belong to the same family of analytical models based on a translation model using a third-order Hermite polynomial. The analytical expression of the classical Hermite model's mean peak factor was proposed in [34] to account for non-Gaussianity of wind processes. The model was further extended to provide an analytical estimate of the standard deviation of the peak factor in [27]. In order to estimate the quantiles, it is assumed here that the distribution of the largest peak values is a Gumbel distribution, which implies a Weibull distribution for the local peaks of the pressure coefficients, as suggested in [42].

$$\mu_{g,H}(T) = k \cdot \left\{ \begin{array}{l} \left(\beta + \frac{\gamma}{\beta}\right) + h_3 \cdot \left(\beta^2 + 2\gamma - 1 + \frac{1.98}{\beta^2}\right) \\ + h_4 \cdot \left[\beta^3 + 3\beta(\gamma-1) + \frac{3}{\beta} \cdot \left(\frac{\pi^2}{6} - \gamma + \gamma^2\right) + \frac{5.44}{\beta^3}\right] \end{array} \right\} \tag{5}$$

$$\sigma_{g,H}(T) = k \cdot \left[\begin{array}{l} \frac{\pi^2}{6\beta^2} + 6.58h_3^2 + 9h_4^2 \cdot \left(1.64\beta^2 + \frac{12.69}{\beta^2} + 5.32\right) + 6.58\frac{h_3}{\beta} \\ + 6h_4 \cdot \left(\frac{2.66}{\beta^2} + 1.64\right) + 12h_3h_4 \cdot \left(1.64\beta + \frac{2.66}{\beta}\right) \end{array} \right]^{\frac{1}{2}} \tag{6}$$

$$X_{g,H}^{\alpha}(T) = \mu_{g,H}(T) - \frac{\sqrt{6}}{\pi} \cdot [\gamma + \ln(-\ln\alpha)] \cdot \sigma_{g,H}(T) \tag{7}$$

in which

$$\begin{cases} h_3 = \frac{\gamma_{c_p}}{4 + 2\sqrt{1 + 1.5\kappa_{c_p}}} \\ h_4 = \frac{\sqrt{1 + 1.5\kappa_{c_p}} - 1}{18} \\ k = \frac{1}{\sqrt{1 + 2h_3^2 + 6h_4^2}} \end{cases} \tag{8}$$

For Gaussian processes, $\gamma_{c_p} = \kappa_{c_p} = h_3 = h_4 = 0$ and $k = 1$; thus Eqs. (5) and (6) reduce to Eqs. (2) and (3), respectively.

The revised Hermite model is a modification of the classical Hermite model, in which the expressions for parameters h_3 and h_4 given in Eq. (8) are substituted by the values $\hat{h}_3$ and $\hat{h}_4$ that minimize the lack-of-fit errors in skewness and kurtosis of the Hermite model [37,44], which are given by:

$$\hat{h}_3 = \frac{\gamma_{c_p}}{6} \cdot \left[\frac{1 - 0.015|\gamma_{c_p}| + 0.3\gamma_{c_p}^2}{1 + 0.2\kappa_{c_p}}\right] \tag{9}$$

$$\hat{h}_4 = \left[\frac{(1 + 1.25\kappa_{c_p})^{\frac{1}{3}} - 1}{10}\right] \cdot \left[1 - \frac{1.43\gamma_{c_p}^2}{\kappa_{c_p}}\right]^{(1 - 0.1\kappa_{c_p}^{0.8})} \tag{10}$$

The analytical solutions for the mean, $\mu_{g,rH}(T)$, and standard deviation, $\sigma_{g,rH}(T)$, of the peak factor using the revised Hermite model are given by Eqs. (5) and (6), respectively, by substituting h_3 with $\hat{h}_3$ and h_4 with $\hat{h}_4$, respectively. The expression for the quantile of the revised Hermite model, $X_{g,rH}^{\alpha}(T)$, is given by Eq. (7) by substituting $\mu_{g,H}(T)$ with $\mu_{g,rH}(T)$ and $\sigma_{g,H}(T)$ with $\sigma_{g,rH}(T)$, respectively. It is noteworthy that the revised Hermite model is valid only for the ranges $0 < \gamma_{c_p} < 12$ and $0 \leqslant \kappa_{c_p}^2 < 2\gamma_{c_p}/3$. In the case in which these conditions on skewness coefficient and excess kurtosis are not satisfied, the revised Hermite model reverts to the classical Hermite model.

The modified Hermite model [45,61] is a modification of the classical Hermite model, in which the shape parameters $\hat{c}_3$ and $\hat{c}_4$ that define the third-order Hermite polynomial of the translation model are related to γ_{c_p} and κ_{c_p} by

$$\gamma_{c_p} = k^3 \cdot (8\hat{c}_3^3 + 108\hat{c}_3 \cdot \hat{c}_4^2 + 36\hat{c}_3 \cdot \hat{c}_4 + 6\hat{c}_3) \tag{11}$$

$$\kappa_{c_p} + 3 = k^4 \cdot \left(\begin{array}{l} 60\hat{c}_3^4 + 3348\hat{c}_4^4 + 2232\hat{c}_3^2 \cdot \hat{c}_4^2 + 60\hat{c}_3^2 + 252\hat{c}_4^2 \\ + 1296\hat{c}_4^3 + 576\hat{c}_3^2 \cdot \hat{c}_4 + 24\hat{c}_4 + 3 \end{array}\right) \tag{12}$$

Eqs. (11) and (12) cannot be inverted analytically and need to be solved numerically; however Yang et al. [61] presented an approximate polynomial solution for $\hat{c}_3$ and $\hat{c}_4$ as functions of to γ_{c_p} and κ_{c_p}. The analytical solutions for the mean, $\mu_{g,mH}(T)$, and standard deviation, $\sigma_{g,mH}(T)$, of the peak factor corresponding to the modified Hermite model are given by Eqs. (5) and (6), respectively, by substituting h_3 with $\hat{c}_3$ and h_4 with $\hat{c}_4$, respectively. Similar to the case of the revised Hermite model, the expression for the quantile of the modified Hermite model, $X_{g,rH}^{\alpha}(T)$, is given by Eq. (7) by substituting $\mu_{g,H}(T)$ with $\mu_{g,mH}(T)$ and $\sigma_{g,H}(T)$ with $\sigma_{g,mH}(T)$, respectively. The region of applicability of the modified Hermite model is defined by $\hat{c}_3^2 + 3\hat{c}_4 \cdot (3\hat{c}_4 - 1) < 0$ [41], which can be approximated in terms of skewness coefficient and excess kurtosis as $-\gamma_{c_p} + (1.25\kappa_{c_p})^2 \leqslant 0$ [62]. If these conditions on $\hat{c}_3$ and $\hat{c}_4$ or on γ_{c_p} and κ_{c_p} are not satisfied, the modified Hermite model reverts to the classical Hermite model.

5.3. Translated-Peak-Process (TPP) model

The TPP model assumes that the pressure coefficient's local peaks follow a Weibull distribution and, thus, that the distribution of the largest peak value is a Gumbel distribution [42]. The TPP model uses a point-to-point mapping between the cumulative distribution function (CDF) of the local peaks for a Gaussian process, which corresponds to a Rayleigh distribution, and the CDF of the local peaks of the considered non-Gaussian process, which corresponds to the assumed Weibull distribution. This mapping procedure is used to estimate the scale and shape parameters, ρ and κ, respectively, of the underlying Weibull distribution, knowing which the statistics of the peak factor can be determined in closed-form as follows:

$$\mu_{g,TPP}(T) = [\rho \cdot \ln(\nu_0 \cdot T)]^{\frac{1}{\kappa}} + \frac{\gamma \cdot [\rho \cdot \ln(\nu_0 \cdot T)^{\frac{1}{\kappa}}]}{\kappa \cdot \ln(\nu_0 \cdot T)} \tag{13}$$

$$\sigma_{g,TPP}(T) = \frac{\pi}{\sqrt{6}} \frac{[\rho \cdot \ln(\nu_0 \cdot T)]^{\frac{1}{\kappa}}}{\kappa \cdot \ln(\nu_0 \cdot T)} \tag{14}$$

$$X_{g,TPP}^{\alpha}(T) = [\rho \cdot \ln(\nu_0 \cdot T)]^{\frac{1}{\kappa}} - \frac{[\rho \cdot \ln(\nu_0 \cdot T)]^{\frac{1}{\kappa}}}{\kappa \cdot \ln(\nu_0 \cdot T)} \cdot \ln(-\ln\alpha) \tag{15}$$

5.4. Liu's model

Liu et al. [24] derived a new moment-based translation model by defining a modified probability density function (PDF) that is symmetric around the median of the original non-Gaussian process. By ordering the experimental data at different instants of time in

increasing values x_i ($i = 1, ..., m, m + 1, ..., N$), where N is the total number of recorded values and $i \geqslant m$ corresponds to values $x_i > m_x$, in which m_x denotes the median of the recorded values, the first four statistical moments of the modified PDF are obtained as follows:

$$\mu_1 = m_x \tag{16}$$

$$\mu_2 = \left[\left(\frac{2}{N-1} \right) \cdot \sum_{i=m}^{N} (x_i - \mu_1)^2 \right]^{\frac{1}{2}} \tag{17}$$

$$\mu_3 = 0 \tag{18}$$

$$\mu_4 = \left(\frac{2}{N-1} \right) \cdot \sum_{i=m}^{N} \left(\frac{x_i - \mu_1}{\mu_2} \right)^4 \tag{19}$$

Using this new PDF, the parameters $\mu_{g,\text{new}}(T)$ and $\sigma_{g,\text{new}}(T)$ are calculated using Eqs. (5) and (6), respectively, with h_3, h_4 and k given by Eq. (8), where γ_{c_p} and κ_{c_p} are substituted with μ_3 and $\mu_4 - 3$, respectively. Finally, the peak factor mean and standard deviation can be obtained as:

$$\mu_{g,L}(T) = \frac{1}{\sigma_{c_p}} \cdot (\mu_2 \cdot \mu_{g,\text{new}}(T) + \mu_1 - \mu_{c_p}) \tag{20}$$

$$\sigma_{g,L}(T) = \frac{\mu_2}{\sigma_{c_p}} \cdot \sigma_{g,\text{new}}(T) \tag{21}$$

It is noted here that Eqs. (17) and (19) are different from those given in the original paper [24], which contain a typographical error, and that Eqs. (20) and (21) were newly derived in order to allow for a direct comparison of peak factor means and standard deviations obtained from different models.

6. Comparison of experimental and analytical peak factor statistics

This section presents a comparison between experimentally measured and analytically estimated statistics of the peak factor for the square HPR considered in this study. First, a comparison of the different analytical models is made by evaluating the percentages of experimental peak factors that have smaller values than different analytical quantiles for an interval of time $T = T_0$ (i.e., for the entire duration of the recorded signals) at different locations on the roof. Second, the different analytical models are compared in terms of estimates of the mean and standard deviation of the peak factors for shorter time intervals. Different error measures are considered and the implications of using these different error measures are discussed. The goal of this section is to identify advantages and limitations of the different analytical models for estimating peak factors for HPRs with respect to location on the roof, wind direction relative to the roof, and duration of the signal. All results are presented only for the Davenport, modified Hermite, TPP, and Liu's models out of the six models described before, i.e., due to space constraints, only the results corresponding to the modified Hermite model are presented among those of the Hermite models. This selection was made because the three Hermite models provided very similar results in all cases and the modified Hermite model was consistently the most accurate of the three Hermite models considered here when compared to the experimental peak factors.

6.1. Comparison of peak factor statistics for $T = T_0$

The comparison of the experimental and analytical peak factor statistics for $T = T_0 = 30$ s (corresponding approximately to a duration of 30 min in full-scale) is performed first for the three wind angles of attack one at the time, after which some synoptic considerations are provided.

6.1.1. Wind angle of attack $\theta = 0°$

Fig. 8 shows the analytical estimates of the peak factor mean for a time interval $T = T_0$ and wind angle $\theta = 0°$. These analytical results can be directly compared to the experimental results for the peak factor g_{T_0} reported in Fig. 5f.

The results reported in Fig. 8a show that the Davenport estimate of the peak factor mean changes very little with the location of the pressure tap, with slightly higher values at the highest point of the roof along the edges parallel to the wind flow (i.e., in zones B and C). The maximum and minimum values are equal to 3.653 and 3.470, respectively. By comparing Fig. 8a and Fig. 5f, it is observed that the Davenport peak factor means significantly underestimate the experimental peak factors in zones A, B, and C, and fail to capture the large peak factor values at the highest points of the roof in zones B and C.

The analytical estimates of the peak factor mean for the modified Hermite models are presented in Fig. 8b. The results of the modified Hermite model are able to reproduce the large values of the experimental peak factors that were observed in the regions where the pressure coefficient process is non-Gaussian, i.e., in zones A, B, and C. The maximum value of the peak factor mean is equal to 8.750; the minimum value of the peak factor mean is equal to 3.014.

The TPP estimates of the peak factor mean are shown in Fig. 8c. The peak factor means have a trend similar to those of the experimental values, with higher values in zones A, B, and C, and the highest values near the highest points of the roof in zones B and C. The maximum and minimum values of the peak factor mean are equal to 6.840 and 3.292, respectively. It is observed that, even though the TPP model is able to identify the regions of non-Gaussianity that are characterized by higher values of the peak factor, it often underestimates the non-Gaussian peak factors, sometimes even significantly.

The Liu's model estimates of the peak factor mean are shown in Fig. 8d. These analytical results present a good agreement with the experimental peak factors shown in Fig. 5f. Similar to the modified Hermite and TPP models, the highest values are obtained in zones A, B, and C. The maximum and minimum values of the peak factor mean are equal to 9.948 and 2.787, respectively. In the non-Gaussian regions, it is observed that these results are very close to those obtained using the modified Hermite model.

It is qualitatively observed that, for $T = T_0$ and $\theta = 0°$, the modified Hermite model provides the best estimates of the experimental peak factors among all models considered here, closely followed by the Liu's model. The TPP model identifies the regions of non-Gaussianity but generally underestimate the peak factors, whereas the Davenport model severely underestimates the peak factors in the non-Gaussian regions of the roof. All models provide very similar results that are close to the experimentally measured peak factors in the middle and in the leeward edge of the roof (i.e., in zones D and E), where the pressure coefficient process can be approximately considered Gaussian.

Fig. 9 shows the analytical estimates of the peak factor standard deviation (scaled up by a factor equal to 10) corresponding to the Davenport, modified Hermite, TPP, and Liu's models for a time interval $T = T_0$ and wind angle $\theta = 0°$. The Davenport estimates of the peak factor standard deviation at the different pressure taps are shown in Fig. 9a. The standard deviation values change very little with the position on the roof. The maximum and minimum values are equal to 0.389 and 0.367, respectively, which correspond to coefficients of variation that are relatively small and slightly higher than 10%.

Fig. 9b reports the peak factor standard deviation estimates obtained using the modified Hermite model. Higher values for the standard deviation are observed near the highest points of the roof in zones B and C (where also the peak factor mean is highest and the pressure coefficient process is strongly non-Gaussian), whereas intermediate values are observed in zone A and the remainder of zones B and C, and lower values are observed in most of zones D and E. The maximum value is equal to 2.121, with coefficients of variation higher than 18% in highly non-Gaussian regions. The minimum value is equal to 0.155.
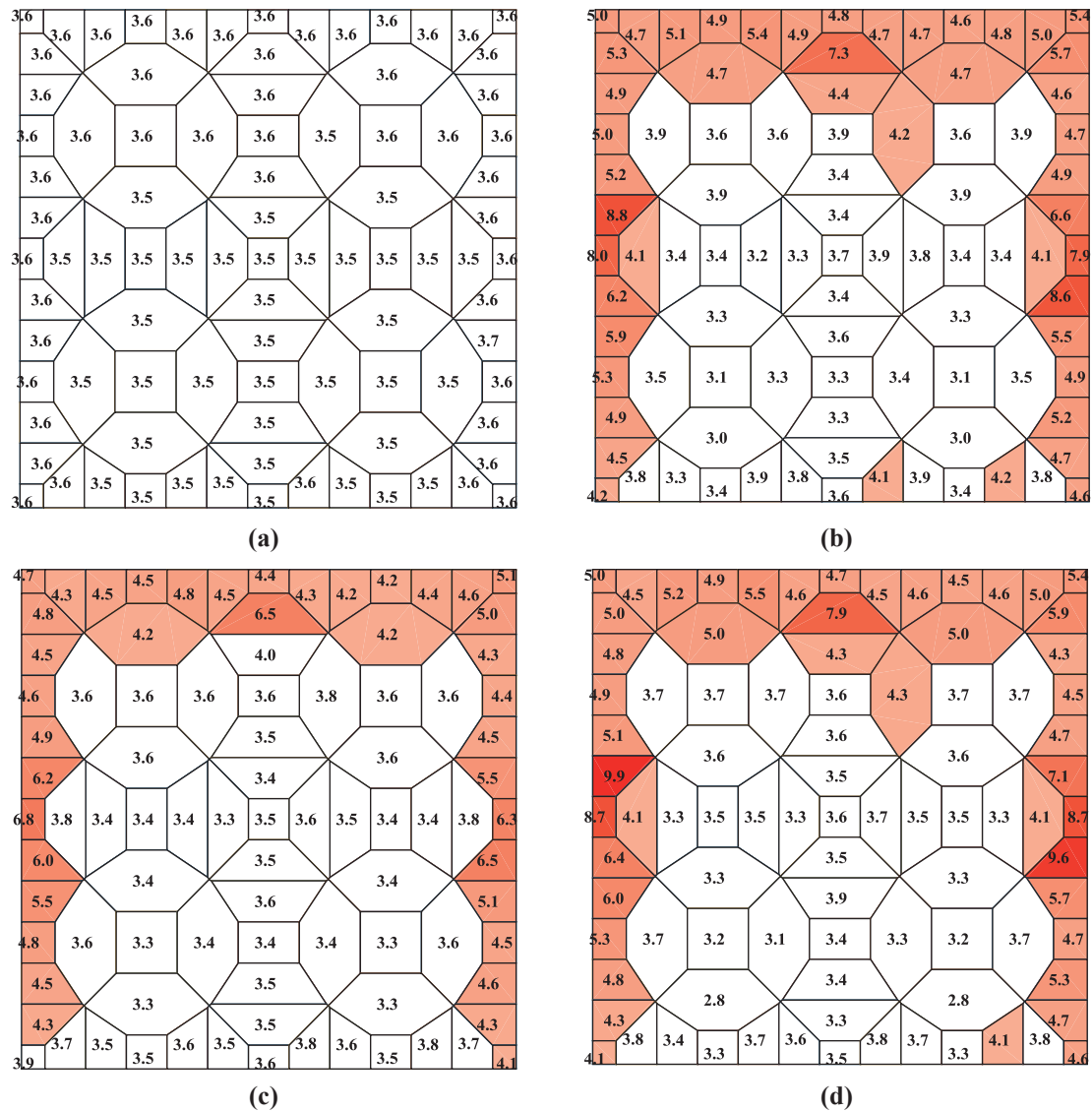
Fig. 8. Analytical estimates of peak factor mean for $T = T_0$ and $\theta = 0°$: (a) Davenport model, $\mu_{g,D}$; (b) modified Hermite model, $\mu_{g,mH}$; (c) TPP model, $\mu_{g,TPP}$; and (d) Liu's model, $\mu_{g,L}$.

The TPP estimates of the peak factor standard deviation are shown in Fig. 9c. The peak factor standard deviations have a trend similar to those of the modified Hermite model, but with a significantly smaller range, i.e., with higher values in zones A, B, and C and lower values in zones D and E. The maximum and minimum values of the peak factor standard deviations are equal to 1.107 and 0.338, respectively, with coefficients of variation close to about 15% in highly non-Gaussian regions.

The Liu's estimates of the peak factor standard deviation are shown in Fig. 9d. The peak factor standard deviations have a trend similar to those of the modified Hermite and TPP models, but with larger maximum values. The maximum and minimum values of the peak factor standard deviations are equal to 2.810 and 0.083, respectively.

Fig. 10 compares the experimental values of the peak factors at each pressure tap with the corresponding analytical estimates of the 90%-confidence intervals (defined as the interval between the 5% and 95% quantiles) of the peak factors for the Davenport, modified Hermite, TPP, and Liu's models. The numbering of the pressure taps reported on the horizontal axis of Fig. 10 corresponds to the numbering shown in Fig. 3. Vertical dashed lines are used to separate the pressure taps in the five different zones identified as A, B, C, D, and E. The experimental

peak factors are identified by red circular markers for pressure taps corresponding to (approximately) Gaussian processes and by green square markers for pressure taps corresponding to non-Gaussian processes.

It is observed that the upper and lower bounds of the 90%-confidence intervals based on the Davenport model are almost constant, with the average value of the 5% quantiles equal to 3.088 and the average value of the 95% quantiles equal to 4.281. The modified Hermite model presents confidence intervals that are significantly wider than those obtained using the Davenport model in zones A, B, C, and a few pressure taps in zone E. These locations correspond to strongly non-Gaussian pressure coefficient processes. In zone D and most of zone E (i.e., where the pressure coefficient processes are approximately Gaussian), the 90%-confidence intervals become very close to those estimated using the Davenport model. Similar observations are made for the TPP and Liu's models when compared to the Davenport model's results. The estimated quantiles are generally lower (particularly the 95% quantile) and the confidence intervals are generally narrower than those obtained from the modified Hermite model for the TPP model. By contrast, the Liu's model provides quantiles that are generally very close to those of the modified Hermite model, except for

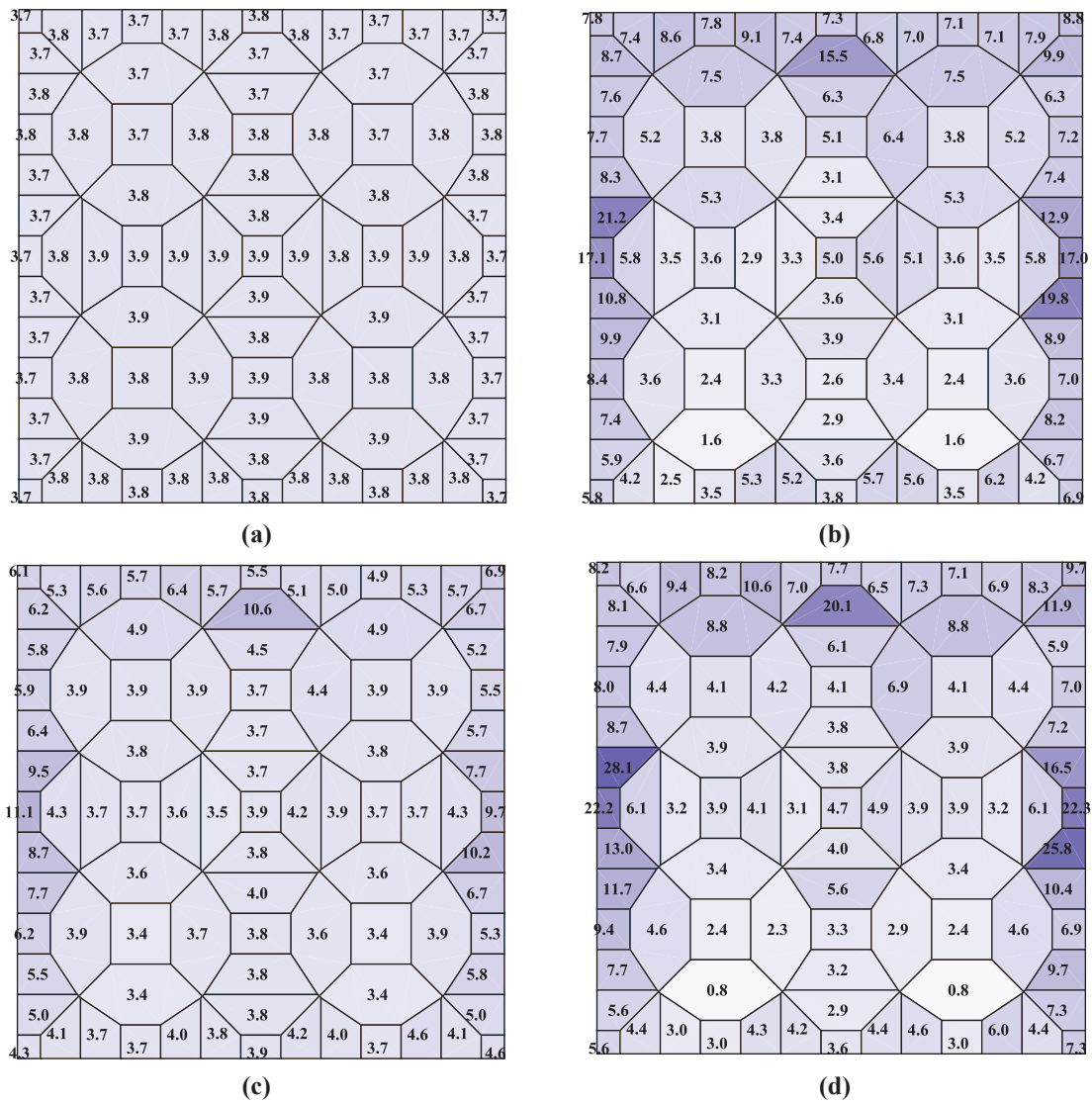**Fig. 9.** Analytical estimates of peak factor standard deviation, scaled up by 10, for $T = T_0$ and $\theta = 0°$: (a) Davenport model, $\sigma_{g,D}$; (b) modified Hermite model, $\sigma_{g,mH}$; (c) TPP model, $\sigma_{g,TPP}$; and (d) Liu's model, $\sigma_{g,L}$.
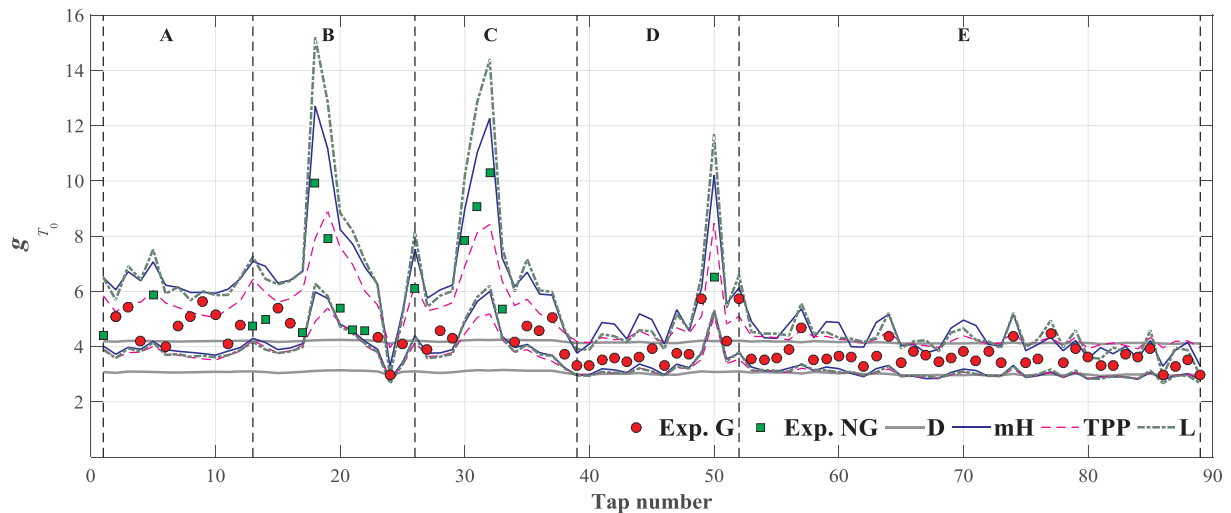

Fig. 10. Comparison between experimental peak factors, g_{T_0}, and analytical peak factor 90%-confidence intervals for $T = T_0$ and $\theta = 0°$.
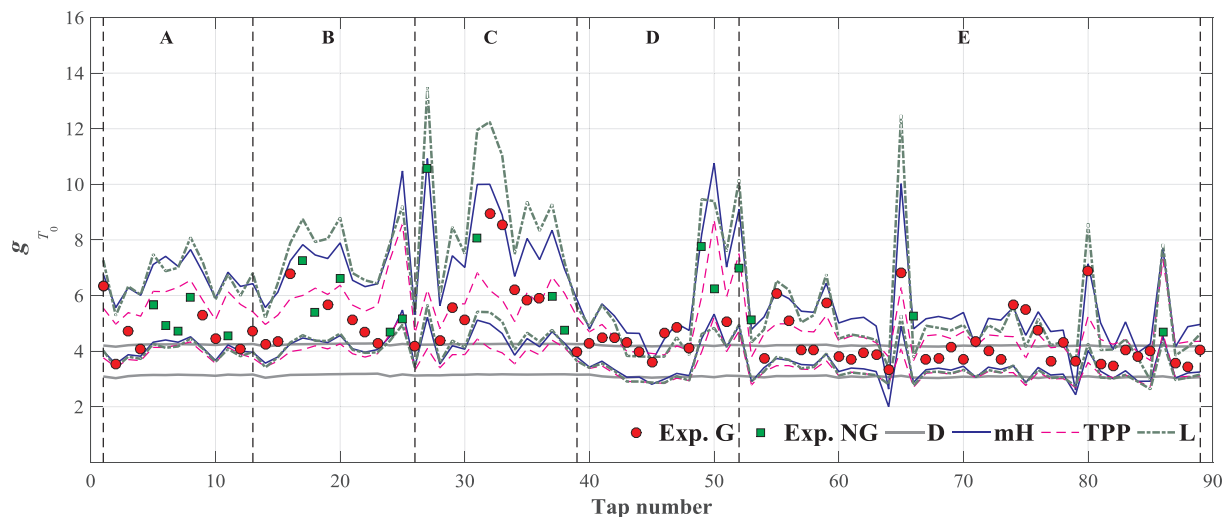
Fig. 11. Comparison between experimental peak factors, g_{T_0}, and analytical peak factor 90%-confidence intervals for $T = T_0$ and $\theta = 45°$.

a few pressure taps where the pressure coefficient process is highly non-Gaussian, where the 95% quantile obtained from the Liu's model is significantly higher than those obtained from the modified Hermite model.

6.1.2. Wind angle of attack $\theta = 45°$

Similar to the case for $\theta = 0°$, the analytical peak factor means and standard deviations were investigated also for $T = T_0$ and $\theta = 45°$. The corresponding maps are not presented here due to space constraints. From these analytical estimates, it is observed that: (1) the Davenport model severely underestimates the peak factors in the non-Gaussian regions of the roof with very small differences of means and standard deviations in Gaussian and non-Gaussian regions; (2) the analytical peak factor means obtained using the modified Hermite model provide the best estimates of the experimental peak factors; (3) the TPP model can identify the regions of non-Gaussianity but generally underestimate the peak factors and have a smaller range of variability of the standard deviations when compared to the Hermite models; (4) the Liu's model gives a satisfactory identification of non-Gaussian regions but generally overestimate the peak factors and presents the largest range of standard deviations. It is noteworthy that, while non-Gaussianity is observed in most of the roof for $\theta = 45°$, the values of the peak factors in these non-Gaussian regions are generally lower than those for $\theta = 0°$, which suggests a lower level of non-Gaussianity.

Fig. 11 compares the experimental peak factors for $T = T_0$ and $\theta = 45°$ with the corresponding analytical estimates of the 90%-confidence intervals of the peak factor at each pressure tap. Also in this case, the 90%-confidence intervals based on the Davenport model are almost constant, significantly lower than the experimental values in non-Gaussian regions, and close to those for $\theta = 0°$. The Liu's model generally presents wider 90%-confidence intervals when compared to other models, followed by the modified Hermite and the TPP models. The modified Hermite, TPP, and Liu's models have significantly wider 90%-confidence intervals than the Davenport model in zones A, B, C, and some parts of zone E (i.e., where the pressure coefficient processes are non-Gaussian); whereas the 90%-confidence intervals for all four models tend to similar values in zone D and the remainder of zone E (i.e., where the pressure coefficient processes are approximately Gaussian). It is also observed that almost all experimental peak factors are contained within the 90%-confidence intervals obtained using the modified Hermite and Liu's models, whereas the TPP 90%-confidence intervals do not include a significant number of experimental peak factors.

6.1.3. Wind angle of attack $\theta = 90°$

The analytical peak factor means and standard deviations obtained for $T = T_0$ and $\theta = 90°$ lead to observations that are qualitatively similar to those made for $\theta = 0°$ and $\theta = 45°$. Also in this case, the corresponding maps are not presented here due to space constraints. As for the previous cases, the Davenport estimates of the peak factor mean are almost constant for all the pressure taps, with the maximum and minimum values that are equal to 3.679 and 3.486, respectively. The modified Hermite estimates of the peak factor mean are close to the experimentally measured peak factors, particularly in zone B, where the pressure coefficient processes are highly non-Gaussian, with a maximum value equal to 7.653 and a minimum value equal to 3.018. The TPP estimates of the peak factor mean are overall in good-to-fair agreement with the experimentally measured peak factors, with the exception of the highest peak factors, which are significantly underestimated by the TPP model. The maximum and minimum values of the peak factor mean based on the TPP model are equal to 6.397 and 3.140, respectively. The Liu's model gives estimates of the peak factor mean that are very close to and generally slightly higher than those of the modified Hermite model, with values ranging between 8.349 and 3.054.

Fig. 12 compares the peak factor experimental values and the analytical estimates of the 90%-confidence intervals of the peak factor at each pressure tap. Also in this case, the 90%-confidence intervals based on the Davenport model are almost constant and close to those for the other wind angles. As observed for other wind angles, the widths of the 90%-confidence intervals in non-Gaussian regions are generally largest for the Liu's model, followed by the modified Hermite model and the TPP model, whereas they are smallest for the Davenport models, for which they are almost constant and close to those observed in Gaussian regions (i.e., most of region C). Almost all experimental peak factors are contained within the 90%-confidence intervals obtained using the modified Hermite and Liu's models, whereas the 90%-confidence intervals obtained using the TPP model fail to capture the largest values of the peak factors.

6.1.4. Synoptic considerations for all wind angles

The empirical distributions of the pressure coefficient local peaks were investigated at all pressure taps for all wind angles in order to verify the assumptions made in the calculation of the confidence intervals for the peak factor, i.e., that the pressure coefficient local peaks follow a Rayleigh distribution in the Davenport model and that they follow a Weibull distribution in all other models. In all cases, a Rayleigh and a Weibull distribution were fitted to the experimental data and a two-sided Kolmogorov-Smirnov test was performed [63].
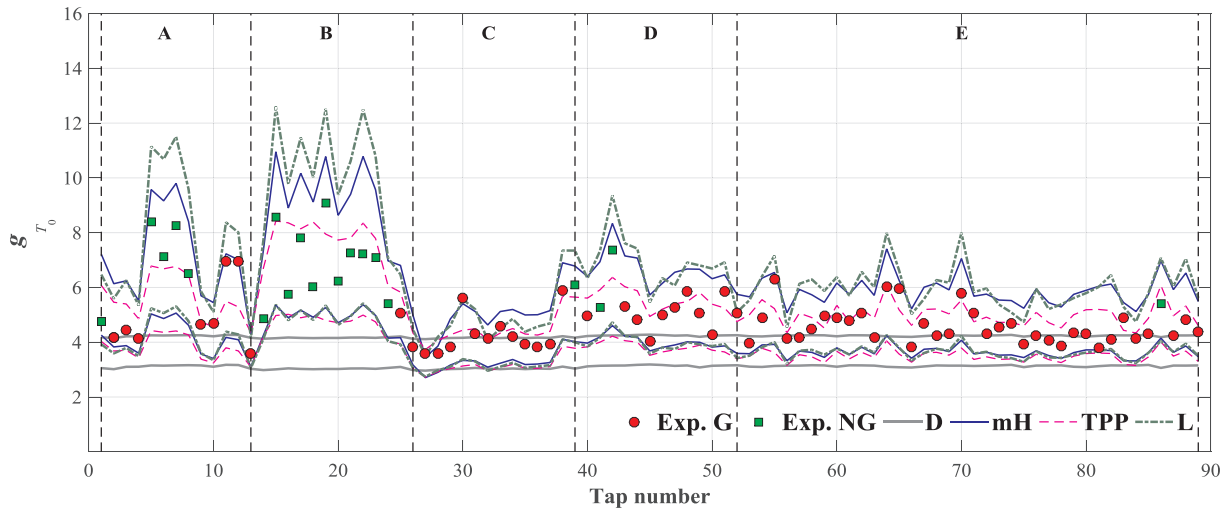
Fig. 12. Comparison between experimental peak factors, g_{T_0}, and analytical peak factor 90%-confidence intervals for $T = T_0$ and $\theta = 90°$.
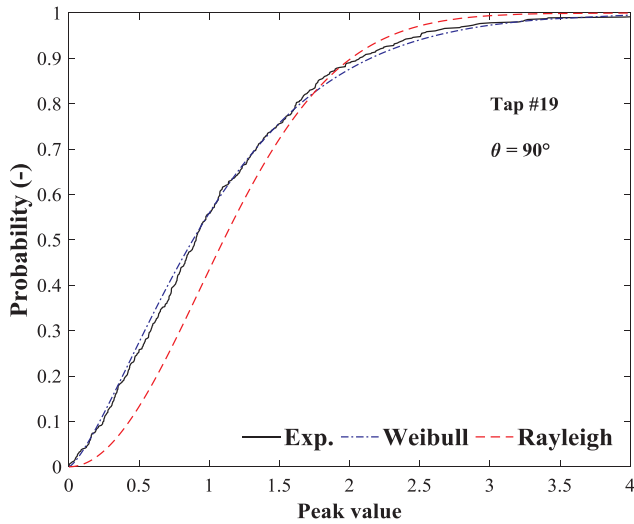

Fig. 13. Cumulative distribution function (CDF) of pressure coefficient peaks at pressure tap #19 for $\theta = 90°$ (highly non-Gaussian case).

It was found that the Weibull distribution could not be rejected with a 5% confidence level in 251 cases out of 267 (i.e., in 94.0% of the cases), whereas the Rayleigh distribution was rejected with a 5% confidence level in all cases. Fig. 13 plots the comparison between the empirical CDF and the fitted Rayleigh and Weibull distributions relative to the pressure coefficient local peaks for the case of pressure tap #19 and $\theta = 90°$. This case corresponds to highly non-Gaussian conditions. It is observed that the Weibull distribution follows very well the empirical CDF, whereas the Rayleigh distribution shows significant differences with the empirical CDF.

These observations confirm that the assumption that the pressure coefficient local peaks follow a Weibull distribution is reasonable. In addition, the Rayleigh distribution was found to differ significantly

from the empirical CDF even for cases in which the pressure coefficient process could be considered approximately Gaussian.

When considering the entire duration of the records (i.e., for $T = T_0$), the experimental peak factors represent single realizations of random variables and cannot be directly compared with the peak factor statistics (i.e., mean and standard deviation) obtained using the different analytical models considered in this study. Thus, in order to provide a quantitative measure of the overall accuracy of the different analytical models for the different wind angles, the analytical estimates of different quantiles $X_M^\alpha(T)$ were compared with the recorded experimental values of the peak factors at each pressure tap.

Table 1 reports the ratios $R_M^\alpha(T)$ (expressed in percentage) of experimental peak factors (over all pressure taps for any given wind angle) that are lower than the analytical quantiles $X_M^\alpha(T)$ for $T = T_0$, M = D, mH, TPP, and L, and α = 95%, 75%, 50%, and 25%. The differences between these quantities and the corresponding α values can be used as a proxy of the overall accuracy of each model in estimating the statistics of the peak factors. In fact, the closer this ratio is to the corresponding value of α, the more accurate the corresponding model can be considered in describing the actual distribution of the peak factors over the entire roof.

As expected, the Davenport model is the least accurate among the models investigated in this study. In fact, the values of $R_D^\alpha(T_0)$ are always significantly lower than α and decrease with increasing wind angle.

The modified Hermite and Liu's models are the most accurate models, even though they tend to overestimate the peak factor values, as indicated by the fact that the values of $R_{mH}^\alpha(T_0)$ and $R_L^\alpha(T_0)$ are systematically higher than the corresponding α, with the only exception of the case for $\alpha = 25\%$ and $\theta = 90°$ for the modified Hermite model. The TPP model tends to underestimate the peak factor values, as indicated by the fact that $R_{TPP}^\alpha(T_0) < \alpha$ for all values of α and all wind angles.

Table 1
Ratios $R_M^\alpha(T_0)$ (in percentage) of experimental peak factors lower than $X_M^\alpha(T_0)$.

θ	D				mH				TPP				L			
	95%	75%	50%	25%	95%	75%	50%	25%	95%	75%	50%	25%	95%	75%	50%	25%
0°	57.3	39.3	15.7	2.2	100.0	85.4	74.2	57.3	87.6	61.8	32.6	6.7	100.0	93.3	68.5	27.0
45°	37.1	15.7	2.2	0.0	94.4	69.7	50.6	29.2	66.3	39.3	16.9	4.5	93.3	82.0	59.6	29.2
90°	28.1	4.5	0.0	0.0	98.9	75.3	39.3	12.4	70.8	32.6	10.1	1.1	100.0	94.4	66.3	25.8

6.2. Comparison of peak factor statistics for $T < T_O$

A comparison of the experimental and analytical peak factor statistics for time intervals that are shorter than the entire pressure coefficients' records was performed to further investigate the relative accuracy of the analytical models considered in this study. This additional comparison allows a direct comparison of the peak factor's statistics evaluated using analytical models and experimental data.

Three smaller time interval lengths were considered, namely $T_1 = T_0/6 = 5$ s (corresponding to approximately 300 s of equivalent-time duration for a full-scale structure), $T_2 = T_0/30 = 1$ s (corresponding to approximately 60 s of equivalent-time duration for a full-scale structure) and $T_3 = T_0/60 = 0.5$ s (corresponding to approximately 30 s of equivalent-time duration for a full-scale structure). The lengths of the shorter intervals were selected so that the entire signal records could be easily divided into a sufficient number of shorter signals of equal length (i.e., into sub-intervals), which could provide reliable estimates of the experimental peak factor means and standard deviations. The experimental peak factors were recorded for each sub-interval and were used to estimate at each pressure tap the sample mean and standard deviation of the peak factor corresponding to the shorter signal duration, based on six, 30, and 60 samples for T_1, T_2, and T_3, respectively. It is noted here that the time intervals considered in this study are shorter than those conventionally used to evaluate maximum wind pressures in wind engineering practice (which are often 10-min or 1-h durations). However, the goal of the present study is to investigate the relative accuracy of different analytical approximations for peak factor statistics when considering different time durations, which can be achieved independently from the specific values of the time durations considered. In fact, once the accuracy of a given analytical method is verified over a range of different time durations, this analytical method can be used to estimate the pressure coefficients corresponding to any time duration of interest with the same accuracy.

By comparing the analytical peak factor statistics of different models for different time durations, it is observed that the peak factor mean increases monotonically for increasing time durations. The peak factor standard deviation strictly decreases for increasing time durations everywhere for the Davenport model and in Gaussian regions for all other models, whereas the peak factor standard deviation does not have a monotonic behavior as a function of the time duration in regions of high non-Gaussianity for all models other than the Davenport model.

The overall accuracy of the different analytical models for the different wind angles was evaluated by estimating the following four different errors for the peak factor means and standard deviations:

(1) the average difference over all the pressure taps between the analytical and experimental estimates of means (ε_1) and standard deviations (δ_1), hereafter referred to as "average error":

$$\varepsilon_1 = \frac{1}{89} \sum_{i=1}^{89} [\mu_{g,M}^{(i)}(T) - \mu_{g,\exp}^{(i)}(T)] \tag{22}$$

$$\delta_1 = \frac{1}{89} \sum_{i=1}^{89} [\sigma_{g,M}^{(i)}(T) - \sigma_{g,\exp}^{(i)}(T)] \tag{23}$$

(2) the root mean squared difference over all the pressure taps between the analytical and experimental estimates of means (ε_2) and standard deviations (δ_2), hereafter referred to as "root mean squared error" (RMSE):

$$\varepsilon_2 = \sqrt{\frac{1}{89} \sum_{i=1}^{89} [\mu_{g,M}^{(i)}(T) - \mu_{g,\exp}^{(i)}(T)]^2} \tag{24}$$

$$\delta_2 = \sqrt{\frac{1}{89} \sum_{i=1}^{89} [\sigma_{g,M}^{(i)}(T) - \sigma_{g,\exp}^{(i)}(T)]^2} \tag{25}$$

(3) the square root of the variation of the mean squared error proposed in [47] for means (ε_3) and standard deviations (δ_3), hereafter referred to as "modified root mean squared error" (mRMSE):

$$\varepsilon_3 = \sqrt{\frac{1}{89} \sum_{i=1}^{89} S_i^2} \tag{26}$$

$$\delta_3 = \sqrt{\frac{1}{89} \sum_{i=1}^{89} Z_i^2} \tag{27}$$

in which:

$$S_i = \begin{cases} \mu_{g,M}^{(i)}(T) - [\mu_{g,\exp}^{(i)}(T) + 2SE_\mu^{(i)}] & \text{if} \quad \mu_{g,M}^{(i)}(T) - \mu_{g,\exp}^{(i)}(T) > 2SE_\mu^{(i)} \\ 0 & \text{if} \quad |\mu_{g,M}^{(i)}(T) - \mu_{g,\exp}^{(i)}(T)| \leqslant 2SE_\mu^{(i)} \\ \mu_{g,M}^{(i)}(T) - [\mu_{g,\exp}^{(i)}(T) - 2SE_\mu^{(i)}] & \text{if} \quad \mu_{g,M}^{(i)}(T) - \mu_{g,\exp}^{(i)}(T) < -2SE_\mu^{(i)} \end{cases} \tag{28}$$

$$Z_i = \begin{cases} \sigma_{g,M}^{(i)}(T) - [\sigma_{g,\exp}^{(i)}(T) + 2SE_\sigma^{(i)}] & \text{if} \quad \sigma_{g,M}^{(i)}(T) - \sigma_{g,\exp}^{(i)}(T) > 2SE_\sigma^{(i)} \\ 0 & \text{if} \quad |\sigma_{g,M}^{(i)}(T) - \sigma_{g,\exp}^{(i)}(T)| \leqslant 2SE_\sigma^{(i)} \\ \sigma_{g,M}^{(i)}(T) - [\sigma_{g,\exp}^{(i)}(T) - 2SE_\sigma^{(i)}] & \text{if} \quad \sigma_{g,M}^{(i)}(T) - \sigma_{g,\exp}^{(i)}(T) < -2SE_\sigma^{(i)} \end{cases} \tag{29}$$

and $SE_\mu^{(i)}$ and $SE_\sigma^{(i)}$ denote the standard errors for the mean and standard deviation, respectively, at pressure tap i;

(4) the percentage average error ratio over all the pressure taps used in [46] for means (ε_4) and standard deviations (δ_4), hereafter referred to as "percentage average error ratio" (PAER):

$$\varepsilon_4 = \frac{1}{89} \sum_{i=1}^{89} \frac{|\mu_{g,M}^{(i)}(T) - \mu_{g,\exp}^{(i)}(T)|}{\mu_{g,\exp}^{(i)}(T)} \cdot 100\% \tag{30}$$

$$\delta_4 = \frac{1}{89} \sum_{i=1}^{89} \frac{|\sigma_{g,M}^{(i)}(T) - \sigma_{g,\exp}^{(i)}(T)|}{\sigma_{g,\exp}^{(i)}(T)} \cdot 100\% \tag{31}$$

These errors were derived from the literature as they are representative of different selections made by different authors. It is noted here that: (1) only few studies in the literature consider the errors on the peak factor standard deviations [42]; (2) only few studies investigate the overall accuracy of different models on an entire roof [46,47]; and (3) the authors were not able to identify any study in the literature that compared the results obtained from different error definitions. The average errors and RMSE are those more commonly used in the literature; however, they present some limitations. In particular, average errors are intuitive and clearly indicate if a model tends to underestimate or overestimate the peak factor statistics; however, they tend to cancel out large errors in opposite directions (i.e., underestimations and overestimations) that are averaged out over many different pressure taps. RMSEs provide an average difference between experimental and analytical results, which provide a better information on how different are analytical and experimental results on the single pressure tap, but loses the information regarding underestimations or overestimations. Both types of errors are affected by the quality of the experimental data, i.e., by the number of samples available to estimate the sample mean and sample standard deviations. The mRMSE was defined here by taking the square root of the error proposed in [47] in order to obtain a quantity with the same dimensions of the average errors and the RMSEs. This error measure minimizes the effects of small sampling size in the experimental data and, thus, can be considered a more reliable error measure than average errors and RMSEs over different time durations. It is noted here that the RMSEs tend to the

Table 2

Peak factor mean's error statistics averaged over all pressure taps for $T = T_1$, T_2, and T_3.

	T	θ	D	mH	TPP	L
ε_1	T_1	0°	−0.579	**−0.027**	−0.186	−0.037
Average error		45°	−0.732	−0.015	−0.295	**−0.011**
		90°	−0.858	**−0.012**	−0.296	0.017
	T_2	0°	−0.376	−0.056	−0.140	−0.070
		45°	−0.444	−0.046	−0.183	−0.054
		90°	−0.509	−0.042	−0.183	**−0.040**
	T_3	0°	−0.342	**−0.104**	−0.176	−0.115
		45°	−0.375	**−0.083**	−0.191	−0.091
		90°	−0.402	−0.061	−0.180	**−0.060**
ε_2	T_1	0°	0.873	**0.236**	0.335	0.252
RMSE		45°	0.885	**0.365**	0.475	0.442
		90°	1.024	**0.250**	0.390	0.317
	T_2	0°	0.444	0.224	**0.201**	0.247
		45°	0.491	**0.253**	0.273	0.298
		90°	0.551	**0.197**	0.229	0.227
	T_3	0°	0.367	0.227	**0.217**	0.243
		45°	0.391	**0.236**	0.254	0.265
		90°	0.417	**0.196**	0.214	0.216
ε_3	T_1	0°	0.400	0.045	**0.039**	0.045
mRMSE		45°	0.326	**0.136**	0.169	0.151
		90°	0.445	0.036	0.082	**0.032**
	T_2	0°	0.243	**0.087**	0.092	0.099
		45°	0.275	**0.123**	0.153	0.150
		90°	0.311	**0.056**	0.097	0.069
	T_3	0°	0.227	**0.125**	0.128	0.137
		45°	0.241	**0.138**	0.163	0.163
		90°	0.256	**0.077**	0.111	0.092
ε_4	T_1	0°	14.2%	**5.6%**	6.5%	**5.6%**
PAER		45°	18.0%	**6.7%**	9.2%	8.3%
		90°	20.5%	**5.0%**	7.8%	6.2%
	T_2	0°	12.8%	6.7%	**6.4%**	7.1%
		45°	14.7%	**6.7%**	7.2%	7.7%
		90°	16.6%	**5.4%**	6.6%	6.1%
	T_3	0°	13.5%	**7.9%**	**7.9%**	8.4%
		45°	14.3%	**7.4%**	8.0%	8.3%
		90°	15.3%	**6.4%**	7.3%	7.0%

Table 3

Peak factor standard deviation's error statistics averaged over all pressure taps for $T = T_1$, T_2, and T_3.

	T	θ	D	mH	TPP	L
δ_1	T_1	0°	−0.087	0.152	**0.037**	0.188
Average error		45°	−0.275	**0.075**	−0.136	0.114
		90°	−0.305	**0.109**	−0.118	0.179
	T_2	0°	**−0.017**	0.203	0.112	0.234
		45°	−0.122	0.192	**0.022**	0.226
		90°	−0.168	0.205	**0.025**	0.265
	T_3	0°	**0.207**	0.298	0.217	0.329
		45°	0.189	0.283	**0.130**	0.317
		90°	0.149	0.301	**0.140**	0.362
δ_2	T_1	0°	0.438	**0.257**	0.316	0.271
RMSE		45°	0.552	0.327	0.448	**0.287**
		90°	0.545	**0.277**	0.363	0.297
	T_2	0°	0.311	0.210	**0.196**	0.254
		45°	0.296	0.230	**0.199**	0.282
		90°	0.328	0.214	**0.144**	0.293
	T_3	0°	0.267	0.297	**0.236**	0.353
		45°	0.225	0.297	**0.191**	0.361
		90°	0.222	0.302	**0.159**	0.394
δ_3	T_1	0°	0.095	0.109	**0.079**	0.113
mRMSE		45°	0.094	0.140	**0.081**	0.117
		90°	0.079	0.105	**0.054**	0.137
	T_2	0°	0.172	0.098	**0.075**	0.103
		45°	0.140	0.119	**0.071**	0.115
		90°	0.165	0.091	**0.029**	0.120
	T_3	0°	0.171	0.194	**0.147**	0.241
		45°	0.122	0.188	**0.102**	0.243
		90°	0.120	0.180	**0.075**	0.267
δ_4	T_1	0°	55.7%	59.2%	**54.5%**	56.8%
PAER		45°	46.0%	56.5%	**44.8%**	49.7%
		90°	39.7%	47.5%	**35.5%**	49.2%
	T_2	0°	32.9%	38.5%	**31.5%**	39.9%
		45°	28.7%	34.2%	**24.5%**	36.8%
		90°	23.4%	32.3%	**17.1%**	36.9%
	T_3	0°	**35.2%**	50.6%	42.1%	52.9%
		45°	**28.4%**	44.2%	29.2%	46.8%
		90°	**18.4%**	43.3%	22.9%	48.6%

mRMSEs when the experimental sampling size is sufficiently large. Finally, the PAERs provide information on the relative errors, which is very intuitive but may be misleading when the peak factor values vary over a wide range, e.g., in the case of roofs with both approximately Gaussian and highly non-Gaussian regions such as those considered in this study.

Table 2 reports the peak factor mean's error statistics averaged over all pressure taps for the different time intervals, wind angles, and models considered in this study. For each case, the smallest error in absolute value is highlighted in bold fonts. It is observed that all methods tend to underestimate the overall peak factor means (as indicated by the negative values of the average errors for all time intervals and wind angles), and this underestimation is most severe in the case of the Davenport model, as expected. The modified Hermite and Liu's models appear to be similarly accurate when considering the average error; however, when other error measures are considered, these errors for the Liu's model are significantly larger than those for the modified Hermite model and are comparable to or slightly higher than those obtained using the TPP model. The PAER are contained between 5.0% and 9.2% for the modified Hermite, TPP, and Liu's models, indicating an accuracy generally acceptable for engineering applications; whereas they are larger for the Davenport model, with values contained between 12.8% and 20.5%. Overall, the modified Hermite model is observed to provide the best estimates of the peak factor means in almost all cases according to all error measures. However, different error measures appear to provide different indications on the relative accuracy of the different models for different time durations, e.g., by looking at average errors alone, it would be difficult

to identify which model between the modified Hermite and Liu's ones is most accurate. It also appears that the mRMSE is the most consistent, among the error measures considered in this study, in identifying the modified Hermite model as the most accurate model overall. Finally, the errors for θ = 45° are consistently higher than those for other angles for each error measure considered here.

Table 3 reports the peak factor standard deviation's error statistics averaged over all pressure taps for the different time intervals, wind angles, and models considered in this study. For each case, the smallest error in absolute value is highlighted in bold fonts.

It is observed that the Davenport model mostly underestimates the peak factor standard deviations, as indicated by the predominant negative values of the corresponding average errors, whereas the modified Hermite and Liu's models tend to overestimate overall the peak factor standard deviations. By comparing the results corresponding to all error measures, the TPP model appears to provide the best overall estimates of the peak factor standard deviations. However, similar to the observations made for the peak factor mean's errors, different error measures give somewhat different indications on the relative accuracy of the different models for different time durations. For example, the PAER indicates that the Davenport model is the most accurate model overall in estimating the peak factor standard deviation for $T = T_3$, which is a counterintuitive and potentially misleading conclusion. In fact, after a closer inspection of the relative absolute errors at each single pressure tap, it was concluded that this result stems from the fact that the PAER systematically discounts the errors in highly non-Gaussian regions (which are larger for the Davenport model when compared to the other models) and amplifies the errors in

approximately Gaussian regions (which are similar among different models). Also in this case, the mRSME appears to provide the most consistent results. Thus, it is suggested that the mRSME should be used when comparing the results obtained from different models over a large number of pressure taps, particularly when a small sample size is used to estimate experimentally the statistics of the pressure coefficient peak factors.

7. Conclusions

This paper investigates the statistics of the pressure coefficients and their peak factors in hyperbolic paraboloid roofs (HPRs), with particular attention to the characterization of the non-Gaussian properties of the peak factors as functions of the position on a square HPR and the relative direction of the wind. Experimental results for wind tunnel tests on a scaled model of a building with a square HPR are reported for three different wind angles of attack (i.e., θ = 0°, 45°, and 90°).

The pressure coefficient processes at different locations on the roof were identified as (approximately) Gaussian or non-Gaussian based on the values of their skewness coefficient and excess kurtosis. For θ = 0° (i.e., for a wind angle of attack parallel to the hogging direction of the roof), the pressure coefficient processes were identified as non-Gaussian along the detachment edge and the two edges that are parallel to the direction of the wind, and as approximately Gaussian elsewhere. The largest values of the skewness coefficients and excess kurtosis were achieved near the highest points of the roof, i.e., near the middle of the two edges parallel to the direction of the wind. For θ = 45° (i.e., for a wind direction that is incident to the corner of the roof), the pressure coefficient processes were classified as non-Gaussian along the two detachment edges (one parallel to the hogging and the other to the sagging direction), along the other edge parallel to the sagging direction, and in a significant portion of the interior of the roof close to the two detachment edges. For θ = 90° (i.e., for a wind direction that is parallel to the sagging direction of the roof), the pressure coefficient processes were highly non-Gaussian along the detachment edge and the two edges parallel to the wind directions, had a non-negligible level of non-Gaussianity in approximately half of the interior of the roof (i.e., behind the detachment edge until approximately the middle of the roof), and were approximately Gaussian elsewhere. These observations were confirmed by the values of the experimental peak factors obtained from the entire record duration $T = T_0 = 30$ s (corresponding to approximately 30 min of pressure coefficient's record for a full-scale structure), which were significantly higher in the regions identified as non-Gaussian than in those identified as approximately Gaussian for all considered wind angles.

The analytical estimates of peak factors' statistics were calculated and compared with the corresponding experimental estimates by using six different analytical models, namely, the Davenport (D), classical Hermite (H), revised Hermite (rH), modified Hermite (mH), Translated-Peak-Process (TPP), and Liu's (L) models. This investigation directly compared the experimental and analytical estimates of different quantiles for the entire duration of the experimental records. It was observed that the modified Hermite and the Liu's models generally provided the most accurate estimates of the peak factors' quantiles, whereas the TPP model generally slightly underestimated the peak factors values and the Davenport model strongly underestimated the peak factors values. Based on the results of a two-sided Kolmogorov-Smirnov test, it was also shown that the pressure coefficient local peaks (i.e., the local maxima in time of the pressure coefficient's experimental records) generally followed a Weibull distribution, whereas the Rayleigh distribution was found to differ significantly from the empirical cumulative distribution function even for cases in which the pressure coefficient process could be considered approximately Gaussian.

Finally, the experimental and analytical peak factor means and standard deviations were compared for three different time durations obtained by subdividing the experimental records into smaller sub-intervals. The accuracy of the analytical estimates was investigated for three different wind angles of attack and four different error measures. It was observed that the modified Hermite model provided the most accurate estimates of the peak factor means overall, whereas the TPP model presented the most accurate estimates of the peak factor standard deviations overall. It was also observed that different error measures could lead to different (sometimes conflicting) conclusions when investigating different time durations. Among the different error measures considered in this study, the modified root mean squared error appeared to be the most reliable error measure, because it was able to reduce the effects of limited experimental sample sizes on the accuracy of the experimental estimates of peak factor means and standard deviations. Thus, it is suggested to use this error measure when assessing the accuracy of analytical models to estimate the peak factor statistics over different pressure taps.

The study presented in this paper represents a first step toward the definition of appropriate ranges and calculation methods for peak factors to be employed in the analysis and design of HPRs commonly used as cost-effective tensile structures. The present research investigated the peak factor statistics only for a single geometry (square roof) under a specified turbulence condition. Further research is needed to generalize the conclusions reported in this paper, e.g., to different geometrical configurations (e.g., roof curvature and building height), different shapes (e.g., rectangular and circular footprints), and different turbulence conditions.

References

[1] Brandt J, Vejre H. Multifunctional landscapes: motives, concepts and perceptions. Brandt J, Vejre H, editors. Multifunctional landscapes, vol. 1. Southampton (MA): WIT Press; 2004. p. 3–33.

[2] Majowiecki M. Tensostrutture: Progetto e Controllo. Milan (Italy): Edizioni Crea; 2004 [in Italian].

[3] Chilton J. Tensile structures-textiles for architecture and design. In: Pöhl G, editor. Textile polymers and composites for buildings. Cambridge (UK): Woodhead Publishing Limited; 2010. p. 229–57.

[4] Beccarelli P. Biaxial testing for fabrics and foils. PoliMI Springer Briefs; 2015 https://doi.org/10.1007/978-3-319-02228-4_2.

[5] CEN. EN 13782: Temporary structures-tent-safety. Brussels (Belgium): Comité Européen de Normalization (CEN); 2005.

[6] ASCE. ASCE/SEI 19-16: Structural applications of steel cables for buildings. Reston (VA, USA): American Society of Civil Engineers (ASCE); 2010.

[7] ASCE. ASCE/SEI 55-10: Tensile membrane structures. Reston (VA, USA): American Society of Civil Engineers (ASCE); 2010.

[8] Huntington CG. The tensioned fabric roof. Reston (VA, USA): American Society of Civil Engineers (ASCE); 2004.

[9] Huntington CG. Tensile fabric structures. design, analysis, and construction. Reston (VA, USA): American Society of Civil Engineers (ASCE); 2013.

[10] Foster B, Mollaert M. The European design guide for tensile surface structures. Brussels (Belgium): TensiNet; 2004.

[11] McAlester V, McAlester L. A field guide to american houses. New York (NY): Alfred and Knopf; 2013.

[12] Strode W, Dean DL. Design, construction and testing of a plywood hyperbolic paraboloid lattice structure. The bulletin of engineering and architecture, vol. 41. Lawrence, MA: University of Kansas Publications; 1958.

[13] Scotta R, Lazzari M, Stecca E, Cotela J, Rossi R. Numerical wind tunnel for aero-dynamic and aeroelastic characterization of bridge deck sections. Comput Struct 2016;167:96–114.

[14] Rizzo F, Sepe V. Static loads to simulate dynamic effects of wind on hyperbolic paraboloid roofs with square plan. J Wind Eng Ind Aerodyn 2015;137:46–57.

[15] Vassilopoulou I, Gantes CJ. Nonlinear dynamic phenomena in a SDOF model of

cable net. Arch Appl Mech 2010;82(10–11):1689–703.

[16] Vassilopoulou I, Gantes CJ. Nonlinear dynamic behavior of saddle form cable nets under uniform harmonic load. Eng Struct 2011;33(10):2762–71.

[17] Vassilopoulou I, Gantes CJ. Vibration modes and natural frequencies of saddle form cable nets. Comput Struct 2012;88(1–2):105–19.

[18] Vassilopoulou I, Petrini F, Gantes CJ. Nonlinear dynamic behavior of cable nets subjected to wind loading. Structures 2017;10:170–83. https://doi.org/10.1016/j.istruc.2017.03.004.

[19] Rizzo F, D'Asdia P, Lazzari M, Procino L. Wind action evaluation on tension roofs of hyperbolic paraboloid shape. Eng Struct 2011;33(2):445–61.

[20] Rizzo F, D'Asdia P, Ricciardelli F, Bartoli G. Characterization of pressure coefficients on hyperbolic paraboloid roofs. J Wind Eng Ind Aerodyn 2012;102:61–71.

[21] Ding J, Chen X. Assessment of methods for extreme value analysis of non-Gaussian wind effects with short-term time history samples. Eng Struct 2014;80:75–88.

[22] Rizzo F. Aerodynamic behavior of tension structures. Milano (Italy): Silvana Editoriale; 2014. ISBN-10: 8836628400.

[23] Liu M, Chen X, Yang Q. Characteristics of dynamic pressures on a saddle type roof in various boundary layer flows. J Wind Eng Ind Aerodyn 2016;150:1–14.

[24] Liu M, Chen X, Yang Q. Estimation of peak factor of non-Gaussian wind pressures by improved moment-based Hermite model. J Eng Mech 2017;143(7):06017006.

[25] Rizzo F, Ricciardelli F. Design approach of wind load for Hyperbolic paraboloid roof with circular and elliptical plan. Eng Struct 2017;139:153–69.

[26] Caracoglia L, Zuo D. Effectiveness of cable networks of various configurations in suppressing stay-cable vibration. Eng Struct 2009;31(12):2851–64.

[27] Kwon D, Kareem A. Peak factors for non-Gaussian load effects revisited. J Struct Eng 2011;137(12):1611–9.

[28] Ciampoli M, Petrini F. Performance-based Aeolian risk assessment and reduction for tall buildings. Probab Eng Mech 2012;28:75–84.

[29] Giaralis A, Petrini F. Wind-induced vibration mitigation in tall buildings using the tuned mass-damper-inerter. J Struct Eng ASCE 2017;143(9):04017127. https://doi.org/10.1061/(ASCE)ST.1943-541X.0001863.

[30] Barbato M, Petrini F, Unnikrishnan VU, Ciampoli M. Performance-based hurricane engineering (PBHE) framework. Struct Saf 2013;45:24–35.

[31] Gumbel EJ. Statistics of extremes. New York, NY (USA): Columbia University Press; 1958.

[32] Davenport AG. Note on the distribution of the largest value of a random function with application to gust loading. Proc Inst Civil Eng 1964;28(2):187–96.

[33] Gurley KR, Tognarelli MA, Kareem A. Analysis and simulation tools for wind engineering. Probab Eng Mech 1997;12(1):9–31.

[34] Kareem A, Zhao J. Analysis of non-Gaussian surge response of tension leg platforms under wind loads. J Offshore Mech Arct Eng 1994;116(3):137–44.

[35] Winterstein SR. Nonlinear vibration models for extremes and fatigue. J Eng Mech 1988;114(10):1772–90.

[36] Grigoriu M. Crossings of non-Gaussian translation processes. J Eng Mech 1984;110(4):610–20.

[37] Winterstein SR, Ude TC, Kleiven G. Springing and slow-drift responses: predicted extremes and fatigue vs simulation. In: Proceedings, behavior of offshore structures at sea - BOSS-94, vol. 3. MIT; 1994. p. 1–15.

[38] Sadek F, Simiu E. Peak non-Gaussian wind effects for database-assisted low-rise building design. J Eng Mech 2002;128(5):530–9.

[39] Tieleman HW, Ge Z, Hajj MR. Theoretically estimated peak wind loads. J Wind Eng Ind Aerodyn 2007;95(2):113–32.

[40] Tieleman HW, Elsayed MAK, Ge Z, Hajj MR. Extreme value distributions for peak pressure and load coefficients. J Wind Eng Ind Aerodyn 2008;96(6–7):1111–23.

[41] Choi M, Sweetman B. The Hermite moment model for highly skewed response with application to tension leg platforms. J Offshore Mech Arct Eng

[42] 2010;132(2):021602.

[42] Huang MF, Lou W, Chan CM, Lin N, Pan X. Peak distributions and peak factors of wind-induced pressure processes on tall buildings. J Eng Mech 2013;139(12):1744–56.

[43] Seo DW, Caracoglia L. Derivation of equivalent gust effect factors for wind loading on low-rise buildings through Database-Assisted-Design approach. Eng Struct 2010;32(1):328–36.

[44] Winterstein SR, Kashef T. Moment-based load and response models with wind engineering applications. J Sol Energy Eng 2000;122:122–8.

[45] Tognarelli MA, Zhao J, Kareem A. Equivalent statistical cubicization for system and forcing nonlinearities. J Eng Mech 1997;123(8):1772–90.

[46] Ma X, Xu F. Peak factor estimation of non-Gaussian wind pressure on high-rise buildings. Struct Des Tall Special Build 2017;26(17):e1386.

[47] Peng X, Yang L, Gavanski E, Gurley K, Prevatt D. A comparison of methods to estimate peak wind loads on buildings. J Wind Eng Ind Aerodyn 2014;126:11–23.

[48] AS/NZS. AS/NZS 1170.2:2002: Structural Design Actions, Part 2: Wind actions. Jointly published by Standards Australia, Sydney (Australia) and Standards New Zealand, Wellington (New Zealand); 2002.

[49] SSEA. Swiss Standard 505 261: Actions on structures -Appendix C: Force and pressure factors for wind. Zurich (Switzerland): Swiss Society of Engineers and Architects (SSEA); 2003.

[50] AIJ. AIJ: Recommendations for loads and building with commentaries, Chapter 6: Wind loads. Tokyo (Japan): Architectural Institute of Japan (AIJ); 2004.

[51] CEN. EN1991-1-4: Eurocode1: Actions on structures - Part 1–4: General Actions, Wind Actions. Brussels (Belgium): Comité Européen de Normalization (CEN); 2005.

[52] ASCE. ASCE 7-10: Minimum design loads for buildings and other structures. Reston (VA, USA): American Society of Civil Engineers (ASCE); 2010.

[53] NRCC. NBCC-4.1.7: Commentary - wind load and effects. Ottawa (Ontario, Canada): National Research Council of Canada (NRCC); 2010.

[54] CNR. CNR-DT207: Guide for the assessment of wind actions and effects on structures. Rome (Italy): National Research Council of Italy (CNR); 2011.

[55] ESA. ES ISO 4354: Wind action on structures – D.3: Wind tunnel testing procedures. Addis Abeba (Federal Democratic Republic of Ethiopia): Ethiopian Standards Agency (ESA); 2012.

[56] BIS. IS 875: Code of practice for design loads for buildings and structures -proposed draft & Commentary, Part3: Wind loads on buildings. New Delhi (India): Bureau of Indian Standards (BIS); 2012.

[57] Luo Y, Huang G, Ding J, Gurley KR. Response to "Revisiting moment-based characterization for wind pressures" by G. Huang, Y. Luo, K.R. Gurley and J. Ding. J Wind Eng Ind Aerodyn 2016;158:162–3.

[58] Suresh Kumar K, Stathopoulos T. Wind loads on low building roofs: a stochastic perspective. J Struct Eng 2000;126(8):944–56.

[59] Huang MF, Huang S, Feng H, Lou WJ. Non-Gaussian time-dependent statistics of wind pressure processes on a roof structure. Wind and Structures 2016;23(4):275–300.

[60] Cartwright DE, Longuet-Higgins MS. Statistical distribution of the maxima of a random function. Proc. R. Soc. London. Ser. A, Math. Phys. Sci. 1956;237(1209):212–32.

[61] Yang L, Gurley KR, Prevatt DO. Probabilistic modeling of wind pressure on low-rise buildings. J Wind Eng Ind Aerodyn 2013;114:18–26.

[62] Winterstein SR, MacKenzie CA. Extremes of nonlinear vibration: comparing models based on moments, l-moments, and maximum entropy. J Offshore Mech Arct Eng 2012;135(2):021602.

[63] Massey FJ. The Kolmogorov-Smirnov test for goodness of fit. J Am Stat Assoc 1951;46(253):68–78.